Geosci. Model Dev. Discuss., 8, 9769–9816, 2015
www.geosci-model-dev-discuss.net/8/9769/2015/
doi:10.5194/gmdd-8-9769-2015
© Author(s) 2015. CC Attribution 3.0 License.

Geoscientific Model Development Discussions
Open Access
EGU

This discussion paper is/has been under review for the journal Geoscientific Model Development (GMD). Please refer to the corresponding final paper in GMD if available.

ISSM-SESAW v1.0: mesh-based computation of gravitationally consistent sea level and geodetic signatures caused by cryosphere and climate driven mass change

S. Adhikari, E. R. Ivins, and E. Larour

Jet Propulsion Laboratory, California Institute of Technology, Pasadena, CA 91109, USA

Received: 9 October 2015 – Accepted: 28 October 2015 – Published: 10 November 2015

Correspondence to: S. Adhikari (surendra.adhikari@jpl.nasa.gov)

Published by Copernicus Publications on behalf of the European Geosciences Union.

Abstract

A classical Green's function approach to computing gravitationally consistent sea level variations, following mass redistribution on the earth surface, employed in contemporary state-of-the-art sea-level models naturally suits the spectral methods for numerical evaluation. The capability of these methods to resolve high wave number features such as small glaciers is limited by the need for large numbers of pixels and high-degree (associated Legendre) series truncation. Incorporating a spectral model into (components of) earth system models that generally operate on an unstructured mesh system also requires cumbersome and repetitive forward and inverse transform of solutions. In order to overcome these limitations of contemporary models, we present a novel computational method that functions efficiently on a flexible mesh system, thus capturing the physics operating at kilometer-scale yet capable of simulating geophysical observables that are inherently of global scale with minimal computational cost. The model has numerous important geophysical applications. Coupling to a local mesh of 3-D ice-sheet model, for example, allows for a refined and realistic simulation of fast-flowing outlet glaciers, while simultaneously retaining its global predictive capability. As an example model application, we provide time-varying computations of global geodetic and sea level signatures associated with recent ice sheet changes that are derived from space gravimetry observations.

1 Introduction

Earth system modeling of climate warming scenarios and their impact on society require ever greater capacity to incorporate the appropriate coupling of models that traditionally have operated in isolation from one another. One example is the necessity to couple the redistribution of earth surface mass and energy during secular and non-secular changes. The coupling of the major ice sheets to the earth's time-varying geoid was a main subject of Erich von Drygalski's PhD thesis (Drygalski, 1887) wherein,

CC BY

along with contemporary work of Woodward (1888), the ability of continental ice mass to attract ocean mass and alter sea level was first discussed and given theoretical treatment. However, the formal modern theory was only expounded almost a century later by Farrell and Clark (1976) who incorporated full accounting of elastic and viscous solid earth deformation on a global scale. This theory is now fully incorporated into the literature for computing past and present-day sea level variations (e.g., Wu and Peltier, 1983; Mitrovica and Peltier, 1991; Mitrovica and Milne, 2003; Riva et al., 2010) and for which contemporary software is available (Spada and Stocchi, 2007).

The importance of gravitational loading and self-attraction on earth system modeling is now demonstrated, for example, via coupling to ocean circulation (Kuhlmann et al., 2011) and ice-sheet models (e.g., Gomez et al., 2013; de Boer et al., 2014), and analysis of earth's rotational variability (Quinn et al., 2015). The solid-earth/sea-level and ice-sheet coupling may be especially important for computation of grounding line migration (e.g., Gomez et al., 2013; Adhikari et al., 2014) and, hence, realistic simulation of fast-flowing outlet glaciers, as it provides direct constraint to important boundary conditions, namely the bedrock elevation and the sea surface height. Conversely, the local and global geodetic and sea level signatures are also highly sensitive to the spatial distribution of ice mass evolution (Mitrovica et al., 2011). It is therefore important to develop a coherent set of models that allows ice sheet projections to simultaneously treat both farfield spatial variability of sea level prediction and local thermal and driving conditions for evolving outlet glaciers.

A major obstacle to efficiently coupling existing models is their fundamentally different computational frameworks: 3-D ice-sheet models operate on an unstructured mesh system (e.g., Gagliardini and Zwinger, 2008; Larour et al., 2012), whereas self-gravitating sea-level models are based on spectral methods (e.g., Mitrovica and Peltier, 1991; Kendall et al., 2005). Any coupling effort, therefore, requires a computationally awkward transform between spectral and spatial domains during the iterative time-steps for computing any single evolutionary projection. Capturing the adjoint properties of the associated mathematical initial/boundary value problems may be a critical

CC BY

property for an ideal numerical architecture to handle the parameter spaces necessary for accurate sea level predictions from 3-D thermomechanical ice-sheet models (e.g., Gagliardini and Zwinger, 2008; Larour et al., 2012). Here we report on a new technique for performing all the computations on an embedded mesh system for a spherical earth provided by Jet Propulsion Laboratory's (JPL) Ice Sheet System Model (ISSM; Larour et al., 2012), while retaining the spatial detail of the ice sheet simulation necessary to examine the rigorous question of grounding line migration and associated non-linear feedbacks with a relatively high degree of local fidelity. This computational framework, which is termed ISSM's Solid Earth and Sea-level Adjustment Workbench (ISSM-SESAW), allows a straightforward and computationally less burdensome numerical approach to be realized.

In Sect. 2, we briefly review the standard Green's function approach to solving the perturbation theory of relative sea level applied to an elastically compressible and density layered self-gravitating, rotating earth. In Sect. 3, we provide our approach to evaluating key components of this theory on an embedded mesh system and demonstrate its superiority (in terms of high-resolution capability, numerical accuracy, and computational efficiency) over contemporary pseudo-spectral methods. As an example model application, in Sect. 4, we produce computations of global geodetic and sea level signatures associated with the recent evolution of polar ice sheets. Finally, in Sect. 5, we summarize key conclusions of this research and briefly outline its scope and limitations.

2 Theory of relative sea level

Redistribution of mass on the earth surface caused by cryosphere and other climate driven phenomena, such as wind stress, ocean currents, and land water storage, perturbs the gravitational and rotational (centrifugal) potential of the planet. Due to the fundamental properties of self-gravitation, perturbation in these potentials induces sea level change, solid earth deformation, and polar motion. If magnitudes (or trends) of mass redistribution are known (e.g., from satellite observations), such important geode-

CC BY

tic signatures can be computed using a simple model for relative sea level variations. Following the seminal work of Farrell and Clark (1976), the so-called self-gravitating postglacial sea-level model for a viscoelastic, rotating earth has been discussed in several papers (e.g., Wu and Peltier, 1983; Mitrovica and Milne, 2003; Kendall et al., 2005; Spada and Stocchi, 2007). Here, we briefly summarize the important (and relevant) components of this model.

For a viscoelastic earth, sea level at a given space on the earth's surface and time may be defined as the difference between the geoid height (i.e., sea surface without any effect of tides and ocean currents and its hypothetical extension to the continents) and the solid earth surface. Small deviations in these variables from the respective initial states, following the mass conserving redistribution of earth's surface or interior materials, may be simply written as follows:

$$S(\theta,\lambda,t) = N(\theta,\lambda,t) - U(\theta,\lambda,t), \tag{1}$$

where S is the change in sea level relative to the initial reference value (termed "relative sea level"), N is the perturbation in geoid radius evaluated at the reference surface ellipsoid, U is the associated radial displacement of the solid earth surface, (θ,λ) are spatial coordinates (on the surface of a spherical earth) that represent colatitude and longitude, and t is time. In a physical sense, Eq. (1) essentially implies that S is the exact variation of sea surface that would be observed on a measuring stick attached to the solid earth surface (Farrell and Clark, 1976; Spada and Stocchi, 2007).

In what follows, we assume that the redistribution of surface mass is induced by transport of material into and out of the cryosphere and that there is an associated viscoelastic gravitational response of the solid earth. For the situation where it is mass transport between continental ice and oceans, it is most convenient to define a loading function, L, so that

$$L(\theta,\lambda,t) = \rho_{\mathrm{I}} H(\theta,\lambda,t) + \rho_{\mathrm{O}} S(\theta,\lambda,t)\mathcal{O}(\theta,\lambda), \tag{2}$$

where H is the change in ice thickness, $\mathcal{O}$ is the so-called ocean function, ρ_{I} is ice density, and ρ_{O} is ocean water density. By definition, $\mathcal{O} = 1$ for oceans and zero otherwise

GMDD
8, 9769–9816, 2015
A new approach to solving the sea-level equation
S. Adhikari et al.

CC BY

(Munk and MacDonald, 1960). This function needs to be introduced in Eq. (2) because S is defined over the whole planet including its continents. (Negative of S in the continents, i.e. $U-N$, may be interpreted as the change in surface elevation with respect to the reference surface ellipsoid.) Note that $\mathcal{O}$ is not an explicit function of time in our development, but would have to be included in cases of significant submergence, or emergence of coastal lands during mass transport (e.g., Johnston, 1993; Milne, 1998).

The mathematical description of the gravity and loading associated with mass transport requires perturbations in gravitational potential, Φ, and rotational potential, Λ, to enter the geoid as follows:

$$N(\theta,\lambda,t) = \frac{1}{g}\left[\Phi(\theta,\lambda,t) + \Lambda(\theta,\lambda,t)\right] + E(t) + C(t), \quad (3)$$

where g is the acceleration due to gravity. Spatial constants appearing above, E and C, are given by

$$\begin{Bmatrix} E(t) \\ C(t) \end{Bmatrix} = -\frac{R^2}{g\rho_O A_O}\int_{\mathbb{S}} \begin{Bmatrix} g\rho_I H(\theta,\lambda,t) \\ \rho_O \overline{C}(\theta,\lambda,t)\mathcal{O}(\theta,\lambda) \end{Bmatrix} \mathrm{d}\,\mathbb{S}, \quad (4)$$

where R is the mean radius of the earth, A_O is the surface area of oceans, $\mathbb{S}$ is the surface domain of a unit sphere, and $\overline{C}$ is a function of potentials and associated deformation of solid earth surface and given by $\overline{C} = \Phi + \Lambda - gU$. Note that eustatic terms E and C are essential to satisfy the mass conservation constraint (Farrell and Clark, 1976). In a hypothetical, non-gravitating (i.e., $\Phi = 0$), non-rotating (i.e., $\Lambda = 0$), rigid (i.e., $U = 0$) earth, E solely describes S and it is this metric that is often termed "sea level equivalent" in order to (alternatively) quantify mass change in glaciers and ice sheets. Sometimes, E by itself is simply termed "eustatic sea level".

Similarly, the viscoelastic gravitational response of solid earth following redistribution of surface mass (Eq. 2) may be partitioned for convenience as follows:

$$U(\theta,\lambda,t) = U_\Phi(\theta,\lambda,t) + U_\Lambda(\theta,\lambda,t), \quad (5)$$

GMDD
8, 9769–9816, 2015

CC BY

where U_Φ and U_Λ are radial displacements of the solid earth surface associated with perturbations in gravitational and rotational potentials, respectively.

In the following, we briefly present the fundamental concepts and mathematical descriptions of gravitational and rotational potentials, as well as the associated deformation of solid earth surface, required to fully define S (Eq. 1). Contemporary models are mostly based on the same theory.

2.1 Gravitational potential and solid earth deformation

The general model description presented above may be applied to any earth model, ranging from a simple rigid earth (e.g., Woodward, 1888) to a comprehensive 3-D viscoelastic earth with lateral heterogeneity and non-linear rheology (e.g., Wu and van der Wal, 2003). Here, we consider earth as a radially stratified elastic sphere, whose short-term responses are characterized by the so-called load Love numbers (Love, 1911; Longman, 1962) that are referred to the Legendre transform spectral representation of the spherical coordinates on the surface of a sphere.

In order to define Φ and U_Φ, we employ a Green's function approach to solving for interior earth responses at the surface, essentially following the load Love number formalism for a seismologically constrained elastic earth (e.g., Longman, 1962; Takeuchi et al., 1962). Let G_Φ and G_U be the non-dimensional Green's functions for a radially stratified, spherically symmetric elastic earth that are respectively associated with Φ and U_Φ. These functions may be represented in the domain of the Legendre transform as follows:

$$\begin{Bmatrix} G_\Phi(\alpha) \\ G_U(\alpha) \end{Bmatrix} = \sum_{l=0}^{\infty} \begin{Bmatrix} 1 + k_l' \\ h_l' \end{Bmatrix} P_l(\cos\alpha), \tag{6}$$

where P_l are Legendre polynomials of degree l (see Appendix A), k_l' and h_l' are the load Love numbers (Longman, 1962), and α is the arc length between the loading point and the evaluation point on the earth's surface. The load Love numbers appear-

GMDD
8, 9769–9816, 2015
A new approach to solving the sea-level equation
S. Adhikari et al.

cc BY

ing above have a simple physical interpretation: P_l is the perturbation in degree l representation of non-dimensional gravitational potential in a Legendre transform space induced by the applied mass itself, whereas $k'_l P_l$ and $h'_l P_l$ are similar perturbations for non-dimensional gravitational potential and non-dimensional radial displacement of the solid earth surface, respectively, caused by the elastic deformation of matter within the earth's interior. Intuitively, $G_\Phi = \sum_{l=0}^{\infty} P_l$ and $G_U = 0$ for a rigid earth model.

The terms $3gG_\Phi / \left[4\pi R^2 \rho_\mathrm{E}\right]$ and $3G_U/(4\pi R^2 \rho_\mathrm{E})$ express the influence of point load of unit mass on the gravitational potential and radial displacement of the solid earth surface respectively (Farrell and Clark, 1976), where ρ_E is the average density of the earth. Spatial convolution of these terms with the loading function (Eq. 2) gives Φ and U_Φ, and we may write

$$\begin{Bmatrix} \Phi(\theta,\lambda,t) \\ U_\Phi(\theta,\lambda,t) \end{Bmatrix} = \frac{3}{4\pi\rho_\mathrm{E}} \int_{\mathbb{S}} \begin{Bmatrix} g\, G_\Phi(\alpha) \\ G_U(\alpha) \end{Bmatrix} L(\theta',\lambda',t)\,\mathrm{d}\mathbb{S}', \tag{7}$$

where (θ',λ') are the variable coordinates. These variable coordinates at which the loading function is defined are related to the fixed ones, (θ,λ), at which Φ and U_Φ are evaluated via α according to the following cosines formula: $\cos\alpha = \cos\theta\cos\theta' + \sin\theta\sin\theta'\cos(\lambda' - \lambda)$.

2.2 Rotational potential and solid earth deformation

The surface mass redistribution and associated deformation of solid earth also induce changes in the earth's rotational vector (e.g., Munk and MacDonald, 1960; Lambeck, 1980; Sabadini et al., 1982). The corresponding change in rotational potential deforms both the solid earth surface and the geoid, thus contributing to a relative sea level signal. Although geological-timescale perturbations to the rotational vector such as true polar wander are governed by glacial isostatic adjustment (GIA) and mantle dynamics (e.g., Spada et al., 1992; Tsai and Stevenson, 2007), short-timescale perturbations such as annual or Chandler wobbles and (decadal to centennial scale) polar drifts are

CC BY

mostly determined by cryosphere and other climate driven mass change (e.g., Gross, 2000; Chen et al., 2013). In the context of mass exchange between continental ice and oceans (Eq. 2), it is therefore important to account for rotational feedbacks in the sea level computation.

In analogy with the description of Φ and U_Φ based on the load Love number theory presented in Sect. 2.1, we may express Λ and U_Λ as follows (e.g., Lambeck, 1980; Milne, 1998):

$$\begin{Bmatrix} \Lambda(\theta,\lambda,t) \\ U_\Lambda(\theta,\lambda,t) \end{Bmatrix} = \sum_{m=0}^{2}\sum_{n=1}^{2} \begin{Bmatrix} 1+k_2 \\ h_2/g \end{Bmatrix} \Lambda_{2mn}(t)\mathcal{Y}_{2mn}(\theta,\lambda), \tag{8}$$

where $\mathcal{Y}_{2mn}$ are degree 2 spherical harmonics (SHs; see Appendix A), Λ_{2mn} are the corresponding SH coefficients, and k_2 and h_2 are degree 2 tidal Love numbers (e.g., Peltier, 1974; Lambeck, 1980). These Love numbers parameterize the elastic response of the solid earth to a potential forcing that does not involve a direct loading on the earth's surface and have a following physical interpretation: $k_2\mathcal{Y}_{2mn}$ is the perturbation in degree 2 order m representation of non-dimensional rotational potential in a SH transform domain caused by the elastic deformation of matter within the earth's interior, and $h_2\mathcal{Y}_{2mn}$ is the same for non-dimensional radial displacement of the solid earth surface. For a rigid earth model, $\Lambda = \sum_{m=0}^{2}\sum_{n=1}^{2}\mathcal{Y}_{2mn}$ and $U_\Lambda = 0$.

In order to define the perturbation Λ_{2mn}, we consider a body fixed right-handed Cartesian coordinates, x_i, with the origin located at the center of mass (CM) of the initially equilibrium earth. (x_1 is aligned along the central meridian and x_3 is positive toward the north pole.) In such a coordinate frame, the products of unperturbed inertia tensor vanish, i.e. $\boldsymbol{I}_{ij} = 0$ (for $i \neq j = 1,2,3$), and the moments of unperturbed inertia tensor for (assumed) rotationally symmetric earth are given by $\boldsymbol{I}_{ii} = \mathcal{A}$ (for $i = 1,2$) and $\boldsymbol{I}_{33} = \mathcal{C}$, where $\mathcal{A}$ is the mean equatorial and $\mathcal{C}$ is the polar moment of inertia. Similarly, the components of (initially equilibrium, and unperturbed) angular velocity vector are given by $\boldsymbol{\omega}_i = \delta_{i3}\Omega$ (for $i = 1,2,3$), where δ_{i3} are the Kronecker deltas and Ω is the mean rotational velocity of the earth. Following the redistribution of mass (Eq. 2), both

GMDD
8, 9769–9816, 2015

CC BY

$\boldsymbol{I}$ and $\boldsymbol{\omega}$ are perturbed from their initial equilibrium states. Let $\mathcal{I}_{ij}$ and $\Omega\,\boldsymbol{m}_i$ be respective perturbation terms, where $\boldsymbol{m}_i$ are non-dimensional and typically of order $\leq 10^{-6}$. Noting the normalization scheme (see Appendix A), Λ_{2mn} may be defined as follows (Munk and MacDonald, 1960; Lambeck, 1980):

$$\Lambda_{201}(t) = \frac{1}{6\sqrt{5}}\Omega^2 R^2 \left[\boldsymbol{m}_1^2(t) + \boldsymbol{m}_2^2(t) - 2\boldsymbol{m}_3^2(t) - 4\boldsymbol{m}_3(t)\right],$$

$$\begin{Bmatrix} \Lambda_{211}(t) \\ \Lambda_{212}(t) \end{Bmatrix} = \frac{-1}{\sqrt{15}}\Omega^2 R^2 \begin{Bmatrix} \boldsymbol{m}_1(t) \\ \boldsymbol{m}_2(t) \end{Bmatrix} [1 + \boldsymbol{m}_3(t)],$$

$$\begin{Bmatrix} \Lambda_{221}(t) \\ \Lambda_{222}(t) \end{Bmatrix} = \frac{-1}{\sqrt{60}}\Omega^2 R^2 \begin{Bmatrix} \boldsymbol{m}_1^2(t - \boldsymbol{m}_2^2(t) \\ 2\boldsymbol{m}_1(t)\boldsymbol{m}_2(t) \end{Bmatrix}. \tag{9}$$

When the rotational perturbations are small, $\boldsymbol{m}_i(t)$ can be determined from the linearized Liouville equations. These then form the general equation of motion for an elastic rotating earth:

$$\begin{Bmatrix} \boldsymbol{m}_1(t) \\ \boldsymbol{m}_2(t) \end{Bmatrix} + \frac{1}{\sigma_r^*}\frac{\mathrm{d}}{\mathrm{d}t}\begin{Bmatrix} -\boldsymbol{m}_2(t) \\ \boldsymbol{m}_1(t) \end{Bmatrix} = \left[\frac{k_s}{k_s - k_2}\right][1 + k_2']\begin{Bmatrix} \psi_1(t) \\ \psi_2(t) \end{Bmatrix}, \tag{10}$$

$$\left\{1 + \frac{4}{3}\frac{[\mathcal{C} - \mathcal{A}]}{\mathcal{C}}\frac{k_2}{k_s}\right\}\frac{\mathrm{d}\boldsymbol{m}_3(t)}{\mathrm{d}t} = [1 + k_2']\,\frac{\mathrm{d}\psi_3(t)}{\mathrm{d}t}, \tag{11}$$

where $\sigma_r^* = \sigma_r[1 - k_2/k_s]$ is the Chandler wobble frequency for an elastic earth, $\sigma_r = \Omega[\mathcal{C} - \mathcal{A}]/\mathcal{A}$ is the same for a rigid earth, $k_s = 3G[\mathcal{C} - \mathcal{A}]/[R^5\Omega^2]$ is the secular (fluid) Love number, and G is the universal gravitational constant. The Love number k_s is a measure of the rotational deformation of a density stratified inviscid earth (Munk and MacDonald, 1960). The variables ψ_i (for $i = 1,2,3$) appearing above are the so-called excitation functions and given by

$$\begin{Bmatrix} \psi_1(t) \\ \psi_2(t) \\ \psi_3(t) \end{Bmatrix} = \frac{1}{\mathcal{C}[\mathcal{C} - \mathcal{A}]}\begin{Bmatrix} \mathcal{C}\,\mathcal{I}_{13}(t) \\ \mathcal{C}\,\mathcal{I}_{23}(t) \\ [\mathcal{A} - \mathcal{C}]\mathcal{I}_{33}(t) \end{Bmatrix} + \frac{1}{\Omega[\mathcal{C} - \mathcal{A}]}\frac{\mathrm{d}}{\mathrm{d}t}\begin{Bmatrix} \mathcal{I}_{23}(t) \\ -\mathcal{I}_{13}(t) \\ 0 \end{Bmatrix}. \tag{12}$$

GMDD
8, 9769–9816, 2015
A new approach to solving the sea-level equation
S. Adhikari et al.

CC BY

Note that the first terms in the right hand side are directly induced by mass redistribution, and hence often called the "mass excitation functions" (Lambeck, 1980).

From the rotational theory presented above, it is clear that Λ_{2mn} and hence Λ and U_Λ can be evaluated completely if three perturbation parameters, namely $\mathcal{I}_{i3}$, are known. In the present context of mass exchange between continental ice and oceans (Eq. 2), we may write (Lambeck, 1980)

$$\begin{Bmatrix} \mathcal{I}_{13}(t) \\ \mathcal{I}_{23}(t) \\ \mathcal{I}_{33}(t) \end{Bmatrix} = -\frac{4\pi R^4}{\sqrt{15}} \begin{Bmatrix} L_{211}(t) \\ L_{212}(t) \\ 2L_{201}(t)/\sqrt{3} \end{Bmatrix}, \quad (13)$$

where L_{2mn} are degree 2 SH coefficients of the loading function.

3 Methods

There are certain elements in the relative sea level theory presented in Sect. 2 that would naturally favor the spectral methods for their numerical evaluation; expansion of non-dimensional Green's functions in the form of an infinite sum of Legendre polynomials (Eq. 6) is one such example. Indeed, contemporary state-of-the-art sea-level models are mostly based on the so-called pseudo-spectral method (Mitrovica and Peltier, 1991) in which all variables appearing in the sea-level equation (SLE) are expanded in the form of SHs and individual SH coefficients are evaluated by satisfying the SLE itself (e.g., Milne, 1998; Mitrovica and Milne, 2003; Spada and Stocchi, 2007).

An alternative to the employed Green's function approach to evaluating (visco)elastic gravitational response of the solid earth (Sect. 2.1) is to consider a comprehensive, 3-D finite-element (FE) modeling of the earth (e.g., Gasperini and Sabadini, 1990; Martinec, 2000). The solid earth response may be parameterized more accurately in this approach by accounting for the lateral heterogeneity and non-linear rheology (e.g., Wu and van der Wal, 2003), but it is mathematically and numerically cumbersome. Therefore, evaluation of SLE that is based on the viscoelastic Love number theory

CC BY

using the pseudo-spectral method in a SH domain has been the standard approach for both standalone modeling of postglacial sea-level and coupling of sea-level and ice-sheet models (e.g., Gomez et al., 2013; de Boer et al., 2014).

Despite the widespread application, one obvious disadvantage of spectral methods is that these require large numbers of terms in the series expansion in order to accurately parameterize a slowly converging function such as G_U (see Sect. 3.1). The associated basis functions (i.e., high degree SHs) have short wavelength signals, which demand uniformly distributed high-resolution pixels over the whole planet. Need for high-degree series truncation in conjunction with high-resolution pixels naturally requires a high computational cost. The same statement applies for capturing high-resolution features such as rapid ice melting from an outlet glacier and adjacent sea level changes: Solutions must be evaluated at large numbers of pixels (as pseudo-spectral methods require equal pixel size over the whole planet) and high-resolution signals can only be resolved with high degree SHs (i.e., high-degree series truncation is essential).

Here we present a simple mesh-based computation of SLE that bypasses the need for SH discretization. As will be shown below, our model yields very accurate solutions, captures (kilometer-scale) high-resolution features for a limited number of elements, and hence is numerically accurate and computationally efficient. Fig. 1 shows an example computational FE mesh of the solid earth surface. This mesh is generated using Gmsh (Geuzaine and Remacle, 2009, http://geuz.org/gmsh/), along with anisotropic mesh refinement based on the Bidimensional Anisotropic Mesh Generator (BAMG) package developed by Hecht (2006). The mesh consists of 16 553 vertices and 33 102 elements. Element sizes are restricted to be in the range of about [60, 1000] km. The mesh refinement metric used in this particular example is a function of the distance from the nearest coastline.

In the following, we summarize our approach to evaluating some important components of relative sea level theory presented in Sect. 2. The relevant model and material parameters are listed in Table 1. Note that we are currently working toward integrat-

CC BY

ing this mesh-based formulation within JPL's ice-sheet model (Larour et al., 2012) and (philosophical and technical) discussion regarding so may be presented in a future publication and is clearly beyond the scope of this paper.

3.1 Evaluation of Φ and U_Φ

Crucial to evaluating Φ and U_Φ is to accurately sample the Green's functions (Eq. 6) that are given in the form of infinite sum of Legendre polynomials. Since $-k'_l$ decays exponentially but h'_l approaches very slowly (see Fig. 2a) toward a constant value as $l \to \infty$, the following discussion focuses on accurate parameterization of G_U. This discussion, however, equally applies to G_Φ as well.

In contemporary models, G_U is evaluated by simply truncating the series at degree $\mathcal{L}$, such that

$$G_U(\alpha) = \sum_{l=0}^{\infty} h'_l P_l(\cos\alpha) \approx \sum_{l=0}^{\mathcal{L}} h'_l P_l(\cos\alpha). \quad (14)$$

Typically, $60 < \mathcal{L} < 600$. For $\mathcal{L} = 128$, for example, the approximation of G_U is characterized by a systematic noise (blue in Fig. 2b) about the exact solution (to be defined later) with higher amplitudes near the loading point, and we may anticipate numerical difficulty in computing changes in bedrock slope or relative sea level near the position of rapidly changing outlet glacier. It is important to note here that we consider the CM of the earth system reference frame (Blewitt, 2003) in our computations, so that degree 1 Love numbers are of the order $h'_1 = -1.29$ and $k'_1 = -1.00$. The same frame is used, for example, for computing gravity fields from the space geodetic satellites.

A much better approximation than Eq. (14) would be the following: We may write

$$G_U(\alpha) = \sum_{l=0}^{\infty} h'_l P_l(\cos\alpha) = h'_\infty \sum_{l=0}^{\infty} P_l(\cos\alpha) + \sum_{l=0}^{\infty} \left[h'_l - h'_\infty\right] P_l(\cos\alpha), \quad (15)$$

GMDD
8, 9769–9816, 2015

CC BY

where h'_∞ is a constant that is reached asymptotically as $l \to \infty$. We now assume that $h'_l = h'_\mathcal{L}$ for all $l \in [\mathcal{L}, \infty)$. Since $\sum_{l=0}^{\infty} P_l(\cos\alpha) = 1/[2\sin(\alpha/2)]$, the above equation becomes

$$G_U(\alpha) \approx \frac{h'_\mathcal{L}}{2\sin(\alpha/2)} + \sum_{l=0}^{\mathcal{L}} \left[h'_l - h'_\mathcal{L}\right] P_l(\cos\alpha). \tag{16}$$

For $\mathcal{L} = 128$, this approximation is free from noise (red in Fig. 2b), and virtually the same as exact solution at least beyond $\approx 1^\circ$ from the point of loading (Fig. 2c). "Exact solution" is obtained by summing over $\mathcal{L} = 10\,000$ (retrieved from http://www.srosat.com/iag-jsg/loveNb.php on 17 August 2015); the first 1800 terms are shown in Fig. 2a.

Since $G_U \to -\infty$ as $\alpha \to 0$, Eq. (16) cannot be evaluated at the point of loading, i.e. at $\alpha = 0$. In order to avoid this inherent singularity, we define the loading function (Eq. 2) at the element centroids and evaluate Green's functions at the vertices so that $\alpha > 0$ for nonzero element size. Let $\mathcal{E}$ and $\mathcal{V}$ be the total number of elements and vertices in the mesh (Fig. 1). For each vertex $v \in [1, \mathcal{V}]$, we compute G_Φ and G_U due to unit loads that are centered at the individual elements $e \in [1, \mathcal{E}]$ as follows:

$$\begin{Bmatrix} \mathbf{G}_\Phi^{ve} \\ \mathbf{G}_U^{ve} \end{Bmatrix} \approx \frac{1}{2\sin(\boldsymbol{\alpha}^e/2)} \begin{Bmatrix} 1 + k'_\mathcal{L} \\ h'_\mathcal{L} \end{Bmatrix} + \sum_{l=0}^{\mathcal{L}} \left[\begin{Bmatrix} k'_l - k'_\mathcal{L} \\ h'_l - h'_\mathcal{L} \end{Bmatrix} P_l(\cos\boldsymbol{\alpha}^e) \right], \tag{17}$$

where variables with superscripts ve are matrices of size $\mathcal{V} \times \mathcal{E}$, and those with e are vectors of size $\mathcal{E} \times 1$. Fig. 2c illustrates how accurately our model samples the exact solution of G_U (i.e., for $\mathcal{L} = 10\,000$) for an example vertex due to the nearby elemental unit loads.

Once $\mathbf{G}_\Phi^{ve}$ and $\mathbf{G}_U^{ve}$ are computed and $L^e(t)$ are given (to be discussed in Sect. 3.3), we may perform the convolution integral (Eq. 7) simply as follows:

$$\begin{Bmatrix} \boldsymbol{\Phi}^v(t) \\ \boldsymbol{U}_\Phi^v(t) \end{Bmatrix} \approx \frac{3}{\rho_\mathrm{E}} \frac{1}{\left[\sum_{e=1}^{\mathcal{E}} A^e\right]} \sum_{e=1}^{\mathcal{E}} \left[\begin{Bmatrix} g\,\mathbf{G}_\Phi^{ve} \\ \mathbf{G}_U^{ve} \end{Bmatrix} L^e(t) A^e \right], \tag{18}$$

GMDD

8, 9769–9816, 2015

A new approach to solving the sea-level equation

S. Adhikari et al.

CC BY

where A^e are elemental areas. Note that variables with superscripts v are vectors of size $\mathcal{V} \times 1$.

3.2 Evaluation of Λ and U_Λ

It is essential to compute L_{2mn} (Eq. 13) and $\boldsymbol{m}_i$ (Eq. 10–11) prior to evaluating Λ and U_Λ. Degree 2 SH coefficients of loading function can be approximated, according to Eq. (A6), as follows:

$$L_{2mn}(t) \approx \frac{1}{\left[\sum_{e=1}^{\mathcal{E}} A^e\right]} \sum_{e=1}^{\mathcal{E}} \left[L^e(t) \mathcal{Y}^e_{2mn} A^e\right], \tag{19}$$

where $\mathcal{Y}^e_{2mn}$ are degree 2 SHs evaluated at elemental centroids (θ^e, λ^e) of the mesh. Here, it is important to note that SH-based computations on an unstructured mesh are valid for low SH degrees, such as $l = 2$, which have very large signal wavelengths.

The system of non-homogeneous ODIs appearing in Eq. (10) can be solved for two unknowns, $\boldsymbol{m}_1$ and $\boldsymbol{m}_2$. The solutions are given by

$$\begin{aligned} \begin{Bmatrix} \boldsymbol{m}_1(t) \\ \boldsymbol{m}_2(t) \end{Bmatrix} &= \begin{bmatrix} \cos\sigma_r^* t & -\sin\sigma_r^* t \\ \sin\sigma_r^* t & \cos\sigma_r^* t \end{bmatrix} \begin{Bmatrix} c_1 \\ c_2 \end{Bmatrix} + \\ &- \frac{\sigma_r}{\Omega(\mathcal{C} - \mathcal{A})} \begin{Bmatrix} \mathcal{J}_{13}(t) - \left[\Omega + \sigma_r^*\right]\left[n_1(t)\cos\sigma_r^* t + n_2(t)\sin\sigma_r^* t\right] \\ \mathcal{J}_{23}(t) - \left[\Omega + \sigma_r^*\right]\left[n_1(t)\sin\sigma_r^* t - n_2(t)\cos\sigma_r^* t\right] \end{Bmatrix}, \end{aligned} \tag{20}$$

where c_1 and c_2 are constants to be determined from initial conditions, and

$$\begin{Bmatrix} n_1(t) \\ n_2(t) \end{Bmatrix} = \int \begin{Bmatrix} \mathcal{J}_{23}(t)\cos\sigma_r^* t - \mathcal{J}_{13}(t)\sin\sigma_r^* t \\ \mathcal{J}_{13}(t)\cos\sigma_r^* t + \mathcal{J}_{23}(t)\sin\sigma_r^* t \end{Bmatrix} \mathrm{d}t. \tag{21}$$

We assume that time-dependent variables may be expressed as the sum of their incremental step changes. For instance, $\mathcal{J}_{i3}(t) = \sum_{k=1}^{K} [\delta \mathcal{J}_{i3}]^k \mathcal{H}(t - t_k)$, where $[\delta \mathcal{J}_{i3}]^k$

GMDD
8, 9769–9816, 2015
A new approach to solving the sea-level equation
S. Adhikari et al.

CC BY

is the incremental step change in moment of inertia over time $t_k \le t < t_{k+1}$ induced by the corresponding incremental step change in applied ice loads and associated sea level variations (Eq. 13), and $\mathcal{H}(t-t_k)$ is a Heaviside step function with magnitude of unity for $t \ge t_k$ and zero otherwise.

If incremental step change in parameters are known a priori (or computed) up to and including K-th time, it is convenient to reset the time so that $\tau = t - t_K$. We may then write, for example, $\mathcal{J}_{i3}(\tau) = \overline{\mathcal{J}}_{i3}\mathcal{H}(\tau)$, where $\overline{\mathcal{J}}_{i3} = \sum_{k=1}^{K}[\delta\mathcal{J}_{i3}]^k$. (For each time interval, we are essentially treating variables as if these can be expressed using a single Heaviside step function.) Substituting t by τ in Eqs. (20) and (21), and a simplification of the latter equation follows

$$\begin{Bmatrix} n_1(\tau) \\ n_2(\tau) \end{Bmatrix} = \frac{1}{\sigma_r^*}\begin{Bmatrix} \overline{\mathcal{J}}_{13}\left[\cos\sigma_r^*\tau - 1\right] + \overline{\mathcal{J}}_{23}\sin\sigma_r^*\tau \\ \overline{\mathcal{J}}_{13}\sin\sigma_r^*\tau - \overline{\mathcal{J}}_{23}\left[\cos\sigma_r^*\tau - 1\right] \end{Bmatrix}\mathcal{H}(\tau). \tag{22}$$

Similarly, the following can be derived from Eq. (11) for $\boldsymbol{m}_3$:

$$\boldsymbol{m}_3(\tau) = c_3 - \frac{[1+k_2']}{\mathcal{C}}\left\{1 + \frac{4}{3}\frac{[\mathcal{C}-\mathcal{A}]}{\mathcal{C}}\frac{k_2}{k_s}\right\}^{-1}\overline{\mathcal{J}}_{33}\,\mathcal{H}(\tau), \tag{23}$$

where c_3 is yet another constant to be determined from initial conditions.

If $\boldsymbol{m}_i$ at $\tau = 0^-$ (i.e., at time $t = t_K$, but just before imposing the K-th incremental change) are known, from Eqs. (20) and (23) we may set $c_i = \boldsymbol{m}_i(0^-)$. Then $\boldsymbol{m}_i$ can be evaluated for any time $\tau \ge 0$. Setting $\tau = t_{K+1} - t_K$, we can compute $\boldsymbol{m}_i(0^-)$ and hence c_i for the subsequent, i.e. $(K+1)$-th, incremental change. For the first incremental change, we impose $\boldsymbol{m}_i(0^-) = 0$ as initial conditions assuming the initial equilibrium state of unperturbed $\boldsymbol{\omega}$.

Once $\boldsymbol{m}_i$ are computed at a given time t, Λ_{2mn} can be easily obtained from Eq. (9), and the evaluation of Λ and U_Λ becomes fairly straightforward as follows:

$$\begin{Bmatrix} \Lambda^v(t) \\ U_\Lambda^v(t) \end{Bmatrix} = \sum_{m=0}^{2}\sum_{n=1}^{2}\begin{Bmatrix} 1+k_2 \\ h_2/g \end{Bmatrix}\Lambda_{2mn}(t)\mathcal{Y}_{2mn}^v, \tag{24}$$

CC BY

where $\mathcal{Y}_{2mn}^{v}$ are degree 2 SHs evaluated at vertices $(\theta^{v}, \lambda^{v})$ of the mesh. Recall that these two quantities are key to computing the rotational feedback.

3.3 Evaluation of other variables

As noted earlier, we define L at the elemental centroids, allowing evaluation of the entire set of variables, including S, at the vertices. Since L depends on S itself (Eq. 2), it is necessary to map S^{v} on to the elemental centroids of the mesh and we do this by simply averaging the corresponding S^{v} for individual elements. We may now write

$$L^{e}(t) = \rho_{\mathrm{I}} H^{e}(t) + \frac{\rho_{\mathrm{O}}}{3} \left[\sum_{v=1}^{3} S^{v}(t) \right]^{e} \mathcal{O}^{e}, \tag{25}$$

where $v = 1, 2, 3$ are the vertices of the eth (triangular) element. In order to evaluate the above equation, $H^{e}(t)$ and $\mathcal{O}^{e}$ must be provided. We define $\mathcal{O}^{e}$ using the Generic Mapping Tools (Wessel et al., 2013) for a set of coordinates $(\theta^{e}, \lambda^{e})$ that define the elemental centroids of the mesh.

Similarly, the eustatic terms appearing in Eq. (4) can be evaluated as follows:

$$\left\{ \begin{matrix} E(t) \\ C(t) \end{matrix} \right\} = - \frac{R^{2}}{g \rho_{\mathrm{O}} \left[\sum_{e=1}^{\mathcal{E}} A^{e} \mathcal{O}^{e} \right]} \frac{4\pi}{3 \left[\sum_{e=1}^{\mathcal{E}} A^{e} \right]} \sum_{e=1}^{\mathcal{E}} \left[\left\{ \begin{matrix} 3 g \rho_{\mathrm{I}} H^{e}(t) \\ \rho_{\mathrm{O}} \left[\sum_{v=1}^{3} \overline{C}^{v}(t) \right]^{e} \mathcal{O}^{e} \end{matrix} \right\} A^{e} \right], \tag{26}$$

where $\overline{C}^{v} = \Phi^{v} + \Lambda^{v} - g \left[U_{\Phi}^{v} + U_{\Lambda}^{v} \right]$ and, as indicated by $[*]^{e}$ inside braces, it is also mapped on to the elemental centroids of the mesh.

Numerical discretization of all components of SLE is now complete, and these can be easily assembled to evaluate radial displacement of the solid earth surface (Eq. 5) as $U^{v}(t) = U_{\Phi}^{v}(t) + U_{\Lambda}^{v}(t)$, perturbation in the geoid height (Eq. 3) as $N^{v}(t) = \left[\Phi^{v}(t) + \Lambda^{v}(t) \right] / g + E(t) + C(t)$, and finally the relative sea level (Eq. 1) as $S^{v}(t) = N^{v}(t) - U^{v}(t)$.

GMDD
8, 9769–9816, 2015

3.4 Solution algorithm and model performance

The computational algorithm used in our mesh-based model is similar to that of pseudo-spectral models (Mitrovica and Peltier, 1991) and is as follows: Since $S^v(t)$ must be known while computing $L^e(t)$ and $S^v(t)$ itself, we employ a recursive scheme with initial solution of $S^v(t)$ obtained by setting $L^e(t) = \rho_l H^e(t)$ (see Eq. 25). It is then feasible to iteratively compute $L^e(t)$ according to Eq. (25) with $S^v(t)$ obtained from the solution of previous iteration. We iterate the simulation until a metric that quantifies the change in two successive solutions is minimal. It takes only a few iterations (typically, five to seven) to converge the solution so that the difference in successive solutions is to within the acceptable accuracy (typically, five order-of-magnitude smaller than the solution itself). This is the standard algorithm for solving the SLE (e.g., Farrell and Clark, 1976; Mitrovica and Peltier, 1991; Spada and Stocchi, 2007) and does not require further explanation.

Once gravitationally consistent solutions for relative sea level, S, are obtained, several useful geodetic parameters may be retrieved easily. Of particular interest, we may compute radial displacement of the solid earth surface, U, from Eq. (5) and perturbation in the geoid height, N, from Eq. (1). Similarly, we can evaluate the following parameters related to the polar motion of the earth: Mass excitation functions, χ_i (for $i = 1,2$), may be computed using the relationship $\chi_i = \mathcal{I}_{i3}/[\mathcal{C} - \mathcal{A}]$; positions of the north pole, (p_1, p_2), in the right-handed Cartesian coordinates may be approximated as $(p_1, p_2) \approx (\boldsymbol{m}_1, \boldsymbol{m}_2)$; and change in the length of a day, ΔD, is given by $\Delta D = -\boldsymbol{m}_3 D$, where $D \approx 86\,400$ s is the length of a solar day. From some of these solutions, we may also infer other useful geodetic observables, such as changes in absolute gravity and geocentric motion of the earth. These will be further discussed in Sects. 4.2 and 4.3.

Most of our computations are done at the vertices of the mesh. Therefore, we have to mainly deal with vectors of size $\mathcal{V} \times 1$. Evaluation of Green's functions, however, requires that matrices of size $\mathcal{V} \times \mathcal{E}$ be considered (Eq. 17), and it naturally demands more computer resources. Fortunately, we can compute Green's functions only once

CC BY

at the beginning as a part of the model initialization because these do not evolve as we simulate the model for an assumed elastic earth. For the mesh considered in this study (Fig. 1), which has $\mathcal{V} = 16\,533$ and $\mathcal{E} = 33\,102$, our Matlab® code takes about 5 min for a serial run in a MacBook Pro (OS X 10.9.5) to compute Green's functions, and less than a minute to evaluate changes in sea level and associated geodetic parameters caused by instantaneous melting of a synthetic ice sheet. The employed unstructured mesh has elements of varying size in the range of about [60, 1000] km. We may vary this range, for instance, to capture high-resolution features in particular locations, say around the Amundsen Sea Sector (ASS), yet the computational cost is minimal as noted above as long as the new unstructured mesh consists of similar $\mathcal{V}$ and $\mathcal{E}$. The lower limit of element size that our model can handle essentially depends on the degree at which series expansion of Green's functions (Eq. 17) is truncated. We use $\mathcal{L} = 10\,000$ for all of our computations. Assuming $\mathcal{P} \approx \pi R/\mathcal{L}$ (Orszag, 1974), where $\mathcal{P}$ denotes the characteristic element size, it implies that our model can capture features of size as small as ≈ 2 km.

There are no standard benchmark (or model intercomparison) experiments available in order to test and validate new postglacial sea level models such as the one presented here. However, for suitable set of experiments, we validate key components of our model by reproducing relevant published results as summarized below (results not shown). We find similar solutions for changes in sea level on a non-rotating elastic earth caused by a change in the total mass of oceans (neglecting ice loads) as computed by Farrell and Clark (1976). Similarly, our model solutions for relative sea level and corresponding changes in geoid height and the solid earth deformation on a non-rotating elastic earth caused by instantaneous melting of a synthetic ice sheet are comparable to corresponding solutions obtained from SELEN, a Fortran 90 program for solving the SLE using a pseudo-spectral method, developed by Spada and Stocchi (2007). We also compare rotation-induced sea level fingerprints to those given in, for example, Mitrovica et al. (2009) and find similar patterns for corresponding experiments.

GMDD
8, 9769–9816, 2015

CC BY

We now provide a brief comparison of our mesh-based model with contemporary pseudo-spectral models in terms of computational efficiency. In the latter models, as noted earlier, the SLE is discretized in the SH domain and individual SH coefficients are evaluated at individual pixels. For a chosen spatial resolution, $\mathcal{P}$, the SH series expansion may be truncated at $\mathcal{L} \approx \pi R/\mathcal{P}$, yielding about $(\pi R/\mathcal{P}+1)^2$ SH coefficients to be computed. In order to sample the SH signals uniformly over the whole planet, pseudo-spectral approach also requires that pixels of equal size be considered. This implies that we must deal with matrices of size $\approx 4\pi R^2/\mathcal{P}^2 \times (\pi R/\mathcal{P}+1)^2$ while evaluating the SLE using pseudo-spectral models. If we are to compute the solutions in spectral formulation, for example, at 60 km resolution along the coastlines as considered in our mesh-based computation, we must deal with matrices of size about $141\,685 \times 111\,947$ (compared to vectors of size $16\,533 \times 1$ required for our model) that certainly demand huge computer resources. In order to compare the model performance systematically, we consider a pseudo-spectral model that is essentially a Matlab® version of SELEN (Spada and Stocchi, 2007) except the following: (1) the earth's surface is pixelized using MEALPix Toolbox that is a Matlab® version of HEALPix (http://healpix.jpl.nasa.gov/), (2) the solid earth is treated as an elastic sphere; and (3) the SLE includes rotational feedback. This Matlab® version of model, coded by the authors (unpublished), is tested and validated against the original SELEN model for suitable experiments. In Table 2, we compare mesh-based and pseudo-spectral models in terms of numerical architecture and computational cost. The latter model already demands a large computer resource even to capture a moderate 51 km resolution. It becomes more cumbersome if we seek to deal with higher wave number features like smaller (kilometer-scale) ice caps and ice fields using pseudo-spectral models, yet there is little degradation in computational efficiency using our mesh-based approach because we can refine the mesh (down to ≈ 2 km) wherever needed while maintaining the similar numbers of vertices in the mesh.

GMDD
8, 9769–9816, 2015

CC BY

4 Some geodetic signatures of ice sheets

Of several climate driven phenomena of mass redistribution on the earth's surface, those related to the cryosphere may be of particular interest. Space based observations have shown that ice sheets and glaciers expell a large volume of melt water in an ongoing climate warming (e.g., Shepherd et al., 2012; Gardner et al., 2013), thus directly contributing to the sea level rise (e.g., Hay et al., 2015). Such trends are likely to persist, if not amplify, throughout this century and beyond as increased atmospheric and oceanic temperatures are generally predicted for future climate change scenarios (e.g., Bamber and Aspinall, 2013; Jevrejeva et al., 2014). Here, as an example model application, we produce computations of some important geodetic signatures associated with the recent evolution of contemporary ice sheets. Observed from space or in terrestrial arrays, these signatures provide diagnostic information about strong shifts in climate (e.g., Chen et al., 2013).

4.1 The GRACE data

The twin Gravity Recovery and Climate Experiment (GRACE) satellites are now a way of monitoring and assessing earth's time-varying gravity field caused by the climate driven surface mass redistribution and transportation of materials within the earth's interior (e.g., Wouters et al., 2014). The GRACE data that are now available at an unprecedented resolution of a few hundreds of kilometers have revolutionized our approach to evaluating, for example, glaciers and ice sheets mass balance (e.g., King et al., 2012; Ivins et al., 2013; Velicogna and Wahr, 2013) and terrestrial hydrological budget (e.g., Wahr et al., 1998; Swenson et al., 2003).

The GRACE data are distributed in the form of Stokes coefficients (Bettadpur, 2012) and upon standard processing of these SH coefficients, with removal of the mantle GIA signal, we can express the relevant geophysical signals in terms of water height equivalent (WHE). In this analysis, we use GRACE Release-05 Level-2 data products provided by the Center of Space Research, the University of Texas at Austin

GMDD
8, 9769–9816, 2015
A new approach to solving the sea-level equation
S. Adhikari et al.

CC BY

(http://www.csr.utexas.edu/grace/RL05.html). The monthly time series of these data are available up to SH degree and order 60, and cover a period from April 2002 to March 2015 (hereafter referred to as the “GRACE period”). There are only partial or no data available for a few months. We fill these data gaps through a simple linear scaling or interpolation between adjacent monthly data as appropriate. We replace degree 1 and degree 2 Stokes coefficients by the values obtained from the analysis of Satellite Laser Ranging (SLR) observations of five passive geodetic satellites (Cheng et al., 2011, 2013a, b). This is particularly important as our computations predict a degree 1 field related to earth’s geocentric motion and degree 2 field related to polar motion.

We compute Stokes coefficient anomalies for further processing by subtracting the corresponding mean values (over the GRACE period) from individual Stokes coefficients. There may be several techniques of varying complexities to process these data (e.g., Swenson and Wahr, 2002; Chen et al., 2006; Chambers and Bonin, 2012), but all of these involve filtering the unphysical North-South striping patterns that are inherently due to the orbital geometry of the satellites (e.g., Ray and Luthcke, 2006), and reducing the so-called leakage effects that mainly operate between the adjacent sources of signal (e.g., Chen et al., 2006). Here, we generally follow the recipe of Ivins et al. (2013) for recovering WHE from these Stokes coefficient anomalies except that we employ a GIA computed by A et al. (2013) and select a rescaling such that the linear trends in ice mass loss from the AIS and GrIS during the GRACE period are -90 and $-240\,\mathrm{Gt\,yr^{-1}}$, respectively. Throughout, we apply a Gaussian smoothing with a 300 km radius. This smoothing radius may be large enough to filter the short-wavelength noise, yet small enough to retain the actual geophysical signals, and is in the range of typical values recommended for variety of applications (Wahr et al., 1998; Swenson et al., 2003).

The temporal and spatial trends in the final products of the AIS and GrIS mass balance are shown in Fig. 3. The amplitudes of temporal variability are higher for the AIS, implying the large seasonal mass turn over there, but it could be also due to large signal amplitudes of the GIA model used (A et al., 2013). A kink is apparent in the AIS data (Fig. 3a); the ice sheet has lost more mass ($-111\,\mathrm{Gt\,yr^{-1}}$) since 2007

GMDD
8, 9769–9816, 2015

CC BY

than during the early period ($-40\,\mathrm{Gt\,yr^{-1}}$). On the other hand, the GrIS was losing the mass more steadily with a little seasonal turn over, but at a much greater pace ($-240\,\mathrm{Gt\,yr^{-1}}$). Spatial distributions of (linear) mass balance trend are shown in Fig. 3b. The figure suggests that the AIS was mostly losing the mass from the ASS at a large rate ($\mathrm{d}H/\mathrm{d}t \leq -10\,\mathrm{cm\,yr^{-1}}$), and also from the Peninsula and Wilkes Land at a more modest rate. Note that the AIS has also gained mass in a few locations; there are clear signals of mass gain (at a rate of about $2\,\mathrm{cm\,yr^{-1}}$) in the northern East Antarctic Ice Sheet (EAIS). The GrIS lost mass at a much greater pace of about $-20\,\mathrm{cm\,yr^{-1}}$, mainly from the south-east sector during the first half of the GRACE period but losses also expanded toward the west later on. Figure 3b also suggests small mass changes in the north and interior of the GrIS during the GRACE period. All these features are generally consistent with other published solutions, for both AIS and GrIS (e.g., Velicogna and Wahr, 2013). However, it is important to note that our primary goal here is to demonstrate the predictive capabilities of our mesh-based model rather than computing precise mass budget solutions for the polar ice sheets.

4.2 Sea level and other variables

The monthly time series of $H(\theta,\lambda,t)$ for both ice sheets are obtained from the GRACE data as discussed above. We force loading of the model by these mass balance solutions for the two major ice sheets. Our model computes monthly solutions for relative sea level, S, radial displacement of solid earth surface, U, and perturbation in geoid height, N. Figure 4 summarizes these solutions for a combined forcing of ice sheets, where we show the linear trends in variables obtained by fitting the corresponding monthly solutions in a least-square sense. Figure 4a depicts the trend in S with following key features: Large rate of sea level drop ($\mathrm{d}S/\mathrm{d}t \leq -3.0\,\mathrm{mm\,yr^{-1}}$) with large wavelengths around the GrIS; the same, but with relatively smaller wavelengths around the ASS; and a moderate rate of sea level rise ($1.5\,\mathrm{mm\,yr^{-1}}$) in the northern EAIS. The blue contours represent the global mean rate (GMR) of sea level rise with magnitude of

GMDD
8, 9769–9816, 2015

CC BY

about 0.91 mm yr^{-1}. The corresponding values for the AIS and GrIS are about 0.25 and 0.66 mm yr^{-1}, respectively. In the regions enclosed by these contours, sea level either falls or remains unchanged or rises at slower than the GMR. In the exterior regions, on the other hand, sea level rises at a higher pace than the GMR.

From ice-sheet modeling point of view, U and N are perhaps more important variables than S itself because these provide direct constraints to two of the important boundary conditions, namely the bedrock elevation and the sea surface height. Figure 4b shows the spatial distribution of linear trend in U, with same general features as observed for S (Fig. 4a) but of opposite sign. The solid earth surface uplift is predicted to occur at a relatively large rate ($dU/dt \geq 2.5$ mm yr^{-1}) around the ASS and GrIS, and subsides at a rather moderate rate of -0.5 mm yr^{-1} around the northern EAIS. The trend in N shows much greater variability in space (Fig. 4c). Here the computation is performed in the CM reference frame and the corresponding Green's function does not change monotonically (unlike those for S and U) as a function of great-circle distance from the loading point. Note in Fig. 2b how G_U, for example, increases monotonically as the evaluation point moves away from the load. The predicted geoid height drops at a rate of $dN/dt \leq -1.0$ mm yr^{-1} around the ASS and GrIS, while a rise is predicted at a similar rate in the northern EAIS and the north Pacific. Generally speaking, the relative sea level, geoid height change and solid earth deformation are linearly related to each other (Eq. 1). Therefore, sea level drop is generally accompanied by the earth surface uplift and sea surface fall, and sea level rise is by the earth surface subsidence and sea surface rise.

It may be useful to evaluate the corresponding changes in absolute gravity (gravity anomaly or disturbance), because this geodetic variable may be measured directly using absolute gravimeters (e.g., James and Ivins, 1998; Crossley et al., 2012) and space geodetic satellites. It may be possible to compute this variable on the same computational mesh as we use for solving the SLE, but it is more readily estimated from the solutions of N in the SH domain. Here we evaluate gravity anomaly, Δg, that

GMDD
8, 9769–9816, 2015

CC BY

could be measured by a gravimeter on the earth's surface as follows (Lambeck, 1980):

$$\Delta g(\theta,\lambda,t) = \frac{4\pi}{3} G \rho_E \sum_{l=0}^{\infty} \sum_{m=0}^{l} \sum_{n=1}^{2} (l-1) N_{lmn}(t) \mathcal{Y}_{lmn}(\theta,\lambda), \quad (27)$$

where N_{lmn} are the SH coefficients of N. The linear trend in Δg is shown in Fig. 4d. As expected, large negative trends are visible around the GrIS and ASS ($\mathrm{d}\Delta g/\mathrm{d}t \leq -1.0\,\mu\mathrm{gal\,yr}^{-1}$) where mass was being lost rapidly during the GRACE period (Fig. 3b). Similarly, in the regions with mass accumulation such as the northern EAIS (Fig. 3b), rising trends in gravity anomaly are predicted, but at a rather moderate rate of $0.5\,\mu\mathrm{gal\,yr}^{-1}$. (A Gaussian filter of 100 km smoothing radius is employed for these plots.)

An interesting exercise is to compare the relative contribution of individual ice sheets to the total sea level change. (Total sea level change, in the context here, is due to the combined mass evolution of both AIS and GrIS.) For such analysis, we select 14 representative tide gauge stations, half of which are located in the Northern Hemisphere. The description of these sites are given in Table 3 and their coordinates on the global map are shown in Fig. 4a. For two representative sites (one for each hemisphere), Fig. 5a shows the explicit evolution of sea level change and relative contribution of AIS and GrIS. In Honolulu, the total sea level rises faster (black line in the figure) than the GMR (red line) throughout the GRACE period. The GrIS contribution at this site is higher (light blue fill) than its contribution to the global mean value (blue line). The AIS influence at this site is similar. This is summarized in the figure inset, in which we compare the average trends in sea level variation: The local contributions of GrIS ($\mathrm{d}S/\mathrm{d}t = 0.82\,\mathrm{mm\,yr}^{-1}$) and AIS ($0.33\,\mathrm{mm\,yr}^{-1}$) are both greater than the corresponding GMRs (i.e., 0.66 and $0.25\,\mathrm{mm\,yr}^{-1}$, respectively), thus resulting in much greater pace of local sea level rise in Honolulu ($1.15\,\mathrm{mm\,yr}^{-1}$) than the GMR ($0.91\,\mathrm{mm\,yr}^{-1}$). On the contrary, the total sea level falls at a rapid pace in the Pine Island Glacier ($-2.88\,\mathrm{mm\,yr}^{-1}$) despite the positive and larger than global mean ($0.82\,\mathrm{mm\,yr}^{-1}$) contribution of GrIS, and it is mainly due to the local gravitational loss (Fig. 4d) associated with a strong loss in ice mass from the ASS (Fig. 3b).

GMDD
8, 9769–9816, 2015

CC BY

Figure 5b summarizes similar comparison for $\mathrm{d}S/\mathrm{d}t$ at other tide gauge stations (see Table 3 and Fig. 4a). Although the figure is self-explanatory, we make brief remarks on some interesting features. In both west coast (San Francisco; N4) and east coast (Virginia Keys; N5) of the continental United States, contributions of AIS are greater and those of GrIS are smaller than the corresponding GMRs. Their combined effects, however, are contrasting: The pace of local sea level rise ($0.93\,\mathrm{mm\,yr^{-1}}$) is slightly higher than the GMR at San Francisco, and the opposite is true for Virginia Keys where sea level rises at a rather modest rate of $0.82\,\mathrm{mm\,yr^{-1}}$. Greatly contrasting rates are predicted at two closely located places, namely Reykjavik (N6) and Newlyn (N7). Since the AIS contributions are similar at both sites, differing signatures in total sea level change are due to the GrIS: The ice sheet has a strong negative contribution at Reykjavik, causing the total sea level to drop at the great rate of $-1.07\,\mathrm{mm\,yr^{-1}}$. Its contribution at Newlyn, on the other hand, is minimal and therefore the total sea level there rises at much slower than the GMR ($0.34\,\mathrm{mm\,yr^{-1}}$). Note that there are other interesting comparisons such as between the eastern (Casey; S5) and western (Rothera; S7) limits of the AIS. At Casey in the EAIS, the AIS contribution is minimal and the total sea level rise ($0.67\,\mathrm{mm\,yr^{-1}}$) is mainly due to the GrIS. However, at Rothera, both ice sheets have similar contributions but of opposite signs, thus resulting in virtually stagnant sea level ($0.05\,\mathrm{mm\,yr^{-1}}$). In the end, it is also worthwhile to report the overwhelmingly great pace of sea level rise ($1.54\,\mathrm{mm\,yr^{-1}}$) at Syowa in the northern EAIS (S4). The AIS contribution is large there, mainly due to the enhanced gravitational pulling (Fig. 4d) associated with the local mass gain (Fig. 3b).

What we have highlighted thus far are the global predictive features that can be efficiently extracted from our flexible FE mesh system. Coupling to a local mesh of ice-sheet model allows a refined and realistic simulation of outlet glacier mass changes to be realized, while simultaneously retaining predictive capability for global coastal sea level with minimal computational effort. In the section that follows we now apply those model predictive features to two important geodynamical observables associated with space geodesy: polar motion and geocentric motion of the earth.

GMDD
8, 9769–9816, 2015

CC BY

4.3 Polar motion and geocentric motion

The redistribution of mass on the earth's surface (Eq. 2) excites changes in the position of the rotational spin axis with respect to fixed positions in the crust. This is also known as changes in "earth orientation", or commonly known as polar motion (Lambeck, 1980), and has important observational ties to the mass imbalance of the earth's two great ice sheets (Douglas et al., 1990). The GMR of sea level rise caused by ice sheets is roughly 1 mm yr^{-1} since about 2005 (Shepherd et al., 2012). If rates increase during the next 80–100 years, sufficient to reach the upper end of estimate of Jevrejeva et al. (2014) for 2100 (≈ 180 cm), then it will be important to have the state-of-the-art data assimilating ice-sheet models, such as ISSM, incorporate such a profoundly fundamental observable. Here we compute some important attributes of polar motion induced by contemporary ice sheets and associated sea level changes during the GRACE period.

Figure 6a and b shows 3-D plots for monthly position of the north pole. Complex interactions between the near annual forcing and Chandler (433 day period) wobble results in a net polar wobble with varying amplitude. This can be seen in the figures for both ice sheets. While wobbling around the mean rotational axis, the pole also drifts away from its initial position as indicated by trend lines in the figures. A kink in the drift direction is apparent for the AIS in about 2007, which may be linked to similar feature observed in mass evolution of the ice sheet (see Fig. 3a).

In order to predict polar drift from our mesh-based computational framework, we evaluate classic mass excitation functions, χ_1 and χ_2, associated with individual ice sheets (Fig. 6c) and the corresponding annual pole positions (Fig. 6d). The north pole in Fig. 6d represents that of year 2002. The mass loss in the GrIS yields positive χ_1 and negative χ_2 in the employed right-handed Cartesian system, implying that the general drift direction is toward the fourth quadrant defined by $x_1 > 0$ and $x_2 < 0$ (see Fig. 6d). Since χ_1 and χ_2 are of similar order of magnitudes, the GrIS induced drift is directed toward the ice sheet itself along $\approx 40^\circ$ W longitude. On the other hand, the combination

GMDD
8, 9769–9816, 2015

CC BY

of rapid mass loss in the ASS and mass gain in the northern EAIS yields positive excitation functions, thus causing the north pole wander vector to be directed toward a Eurasian ≈ 60° E longitude. Since the AIS and GrIS operate in-phase for χ_1 and out-of-phase for χ_2, their combined effects would amplify the former excitation function and shrink the latter one. Consequently, the pole would be drifting along ≈ 15° W longitude during the GRACE period as shown in Fig. 6d.

These predictions are generally consistent with the report by Chen et al. (2013): Glaciers and ice sheets explain a large fraction of observed χ_1 during 2005–2011 but their contributions to χ_2 are minimal. We find $d\chi_1/dt = 2.87 \pm 0.15\,\mathrm{mas\,yr^{-1}}$ for the same period, which is approximately half the trend attributed by Chen et al. (2013) to glaciers and ice sheets. Large rates of mass loss from other glaciated regions such as the high-altitude Himalayas (Gardner et al., 2013) may explain the discrepancy, although more rigorous effort is needed to justify this. Despite the minimal collective contributions of glaciers and ice sheets to the observed trend in χ_2, it is important to highlight the significant role that the AIS is playing to counter the GrIS induced negative χ_2 (see Fig. 6c). Rapid mass loss from the ASS, aided by the mass gain in the northern EAIS, is responsible for drifting the pole along ≈ 15° W longitude, which would otherwise be heading the GrIS. Observations of further eastward motion of the pole (along ≈ 15° E longitude; Fig. 6d) may be explained by mass transport and other excitations unrelated to ice sheets.

From gravitationally consistent surface mass redistribution, the mesh model may also estimate the geocentric motion of the earth. While observationally more elusive than polar motion, this is a fundamental parameter important to global reference frames. The geocentric motion is caused by the shift in relative position between the CM of the earth system and the center of figure (CF) of the solid earth surface, and this information is essential to reconcile the geodetic data that are tracked from the ground stations using absolute gravimeters and also from the passive geodetic satellites using SLR. Let the CM-CF shift is denoted by the position vector $\boldsymbol{X}_i$ (for $i = 1, 2, 3$) in the right-handed Cartesian system. The components of this vector can be computed from the degree 1

CC BY

SH coefficients of gravitationally consistent loading function (Eq. 2) as follows (e.g., Wu et al., 2006):

$$\boldsymbol{X}_i(t) = \frac{\sqrt{3}}{\rho_\mathrm{E}}\left[1 - \frac{h'_1 + 2l'_1}{3}\right]\left[L_{111}(t)\delta_{1i} + L_{112}(t)\delta_{2i} + L_{101}(t)\delta_{3i}\right], \tag{28}$$

where δ_{1i}, δ_{2i} and δ_{3i} are the Kronecker deltas, and l'_1 is the degree 1 load Love number, just like h'_1 and k'_1, and in the employed CM reference frame is of the order $l'_1 = -0.89$ (Blewitt, 2003).

The ice sheet induced components of $\boldsymbol{X}$ during the GRACE period are plotted in Fig. 7. Since both ice sheets are located near the poles (i.e., with small $|x_i|$ for $i = 1,2$ and large $|x_3|$), their individual contributions to the CM-CF shift are naturally larger for $\boldsymbol{X}_3$, which is associated with degree 1 zonal harmonic. However, the ice sheets have secular trends in this component of geocentric motion that oppose one another. This opposition mutes their combined signal (Fig. 7c) predicting a gradual shift toward the south pole at a rate of $-0.44 \pm 0.03\,\mathrm{mm\,yr^{-1}}$. Both seasonal amplitudes and secular trends in horizontal components of the geocentric motion, i.e. $\boldsymbol{X}_1$ and $\boldsymbol{X}_2$, are quite minimal, compared with the corresponding solutions inferred from the SLR observations (Cheng et al., 2013b), despite the in-phase functioning of ice sheets for the latter component. Incorporation of degree 1 predictions in ice-sheet models such as ISSM will be important for considering geodetic reference frame stability, but it is unlikely to be relegated to the status of a data assimilation parameter due to problems with inferring decadal time-scale CM-CF drift (Ries, 2013), especially when compared to other global space geodetic observables.

5 Conclusions

Toward developing a coherent set of ice-sheet and solid-earth/sea-level models that operates on a common computational architecture provided by JPL's ISSM (https:

GMDD
8, 9769–9816, 2015

//issm.jpl.nasa.gov/), we present a novel approach to evaluating gravitationally consistent relative sea level and associated geodetic variables. Unlike contemporary sea-level models that are based on SH formulation, the model can function efficiently on a flexible (un)structured FE (or finite-difference) mesh system, thus capturing the physics operating at kilometer-scale yet capable of simulating geophysical quantities that are inherently of global scale with minimal computational cost. In order to explain the global model, we compute evolution of sea level fingerprints and other observables, such as geoid height, gravity anomaly and solid earth deformation, associated with GRACE inferred monthly mass balance of ice sheets for a period from April 2002 to March 2015 in a manner that is broadly familiar to the space geodesy and altimetry communities (e.g., Farrell and Clark, 1976; Riva et al., 2010; Mitrovica et al., 2011). We also evaluate the corresponding polar and geocentric motion of the earth and find that both ice sheets play a significant role in explaining the observed eastward drift of the north pole since about 2005 (Chen et al., 2013), whereas the predicted influences on earth's geocentric motion are minimal compared with the SLR inferred estimates (Cheng et al., 2013b).

Relevant global geodetic and sea level signatures that can be computed using the mesh-based model presented in this study for earth system modeling are numerous. Coupling global sea-level model to a local mesh of 3-D ice-sheet model, for example, enhances the realistic simulation of outlet glaciers, such as Pine Island Glacier, as it provides direct constraint to two of the important boundary conditions, namely the bedrock elevation and the sea surface height, that would be consistent with global scale climate driven mass redistribution. There may yet be several other applications that involve continental scale gravitational and loading interaction. However, the current model development is strictly applied to an elastically compressible and density layered self-gravitating earth and, hence, suitable for short-timescale (monthly to decadal) evaluation of variables. For relatively long-timescale (centennial or longer) computations, the model should also account for viscoelastic response of the solid earth. It may be achieved through appropriate parameterization of long-term GIA response via time-dependent viscoelastic Love numbers.

GMDD
8, 9769–9816, 2015

CC BY

Code availability

In the Supplement, we provide source code and necessary dataset to run the model within JPL's ISSM (https://issm.jpl.nasa.gov/) and reproduce some of the results (particularly those related to the AIS).

Appendix A: SHs and Legendre polynomials

Any square-integrable function, $f(\theta,\lambda,t)$, can be expanded as the infinite sum of SHs, i.e.

$$f(\theta,\lambda,t) = \sum_{l=0}^{\infty}\sum_{m=0}^{l}\sum_{n=1}^{2} f_{lmn}(t)\mathcal{Y}_{lmn}(\theta,\lambda), \tag{A1}$$

where f_{lmn} are SH coefficients and $\mathcal{Y}_{lmn}$ are (real) 4π-normalized SHs of degree l and order m. These SHs may be expressed in terms of associated Legendre polynomials, P_{lm}, as follows:

$$\mathcal{Y}_{lmn}(\theta,\lambda) = \sqrt{[2-\delta_{0m}]\,[2l+1]\frac{[l-m]!}{[l+m]!}}\,P_{lm}(\cos\theta)[\delta_{1n}\cos m\lambda + \delta_{2n}\sin m\lambda], \tag{A2}$$

where δ_{0m}, δ_{1n} and δ_{2n} are the Kronecker deltas. For $x \in [-1,1]$, polynomials $P_{lm}(x)$ are given by

$$P_{lm}(x) = (1-x^2)^{m/2}\frac{\mathrm{d}^m P_l(x)}{\mathrm{d}x^m}, \tag{A3}$$

where

$$P_l(x) = \frac{1}{2^l\ l!}\frac{\mathrm{d}^l(x^2-1)^l}{\mathrm{d}x^l} \tag{A4}$$

GMDD
8, 9769–9816, 2015
A new approach to solving the sea-level equation
S. Adhikari et al.

CC BY

are the Legendre polynomials. This definition of SHs and their normalization are consistent with those employed for GRACE data generation (Bettadpur, 2012). If the function $f(\theta,\lambda,t)$ represents the perturbation in geoid height evaluated at the reference surface ellipsoid so that $Rf(\theta,\lambda,t) = N(\theta,\lambda,t)$, the corresponding SH coefficients f_{lmn} are essentially the so-called "Stokes coefficients" and are often denoted by $C_{lm}(\equiv f_{lm1})$ and $S_{lm}(\equiv f_{lm2})$.

For the chosen 4π normalization scheme, SHs obey the following orthogonality relationship:

$$\int_{\mathbb{S}} \mathcal{Y}_{lmn}(\theta,\lambda)\mathcal{Y}_{l'm'n'}(\theta,\lambda)\,\mathrm{d}\,\mathbb{S} = 4\pi\delta_{ll'}\delta_{mm'}\delta_{nn'}, \tag{A5}$$

where $\delta_{ll'}$, $\delta_{mm'}$ and $\delta_{nn'}$ are once again the Kronecker deltas. If $f(\theta,\lambda,t)$ is known a priori, its SH coefficients can be computed using Eq. (A5) as follows:

$$f_{lmn}(t) = \frac{1}{4\pi}\int_{\mathbb{S}} f(\theta,\lambda,t)\mathcal{Y}_{lmn}(\theta,\lambda)\,\mathrm{d}\,\mathbb{S}. \tag{A6}$$

We employ this property while evaluating, for example, L_{2mn} (see Eq. 19).

The Supplement related to this article is available online at doi:10.5194/gmdd-8-9769-2015-supplement.

Acknowledgements. This research was carried out at the Jet Propulsion Laboratory, California Institute of Technology, under a contract with the National Aeronautics and Space Administration (NASA) and funded through both the Cryosphere Program and the Earth Surface and Interior Focus Area as part of the GRACE Science Team and NASA Sea-level Change Team efforts. Support for S. Adhikari is through a fellowship from the NASA Post-Doctoral Program. Conversations with Richard Gross are acknowledged.

References

A, G., Wahr, J., and Zhong, S.: Computations of the viscoelastic response of a 3-D compressible Earth to surface loading: an application to Glacial Isostatic Adjustment in Antarctica and Canada, Geophys. J. Int., 192, 557–572, doi:10.1093/gji/ggs030, 2013. 9790

Adhikari, S., Ivins, E. R., Larour, E., Seroussi, H., Morlighem, M., and Nowicki, S.: Future Antarctic bed topography and its implications for ice sheet dynamics, Solid Earth, 5, 569–584, doi:10.5194/se-5-569-2014, 2014. 9771

Bamber, J. L. and Aspinall, W. P.: An expert judgement assessment of future sea level rise from the ice sheets, Nature Clim. Change, 3, 424–427, 2013. 9789

Bettadpur, S.: GRACE 327-742, UTCSR Level-2 Processing Standards Document for Level-2 Product Release 0005, Tech. rep., The University of Texas at Austin, Texas, USA, 2012. 9789, 9800

Blewitt, G.: Self-consistency in reference frames, geocenter definition, and surface loading of the solid Earth, J. Geophys. Res., 108, B22103, doi:10.1029/2002JB002082, 2003. 9781, 9797

Chambers, D. P. and Bonin, J. A.: Evaluation of Release-05 GRACE time-variable gravity coefficients over the ocean, Ocean Sci., 8, 859–868, doi:10.5194/os-8-859-2012, 2012. 9790

Chen, J. L., Wilson, C. R., and Seo, K. W.: Optimized smoothing of Gravity Recovery and Climate Experiment (GRACE) time-variable gravity observations, J. Geophys. Res., 111, B06408, doi:10.1029/2005JB004064, 2006. 9790

Chen, J. L., Wilson, C. R., Ries, J. C., and Tapley, B. D.: Rapid ice melting drives Earth's pole to the east, Geophys. Res. Lett., 40, 2625–2630, doi:10.1002/grl.50552, 2013. 9777, 9789, 9796, 9798, 9815

Cheng, M., Ries, J. C., and Tapley, B. D.: Variations of the Earth's figure axis from satellite laser ranging and GRACE, J. Geophys. Res., 116, B01409, doi:10.1029/2010JB000850, 2011. 9790

Cheng, M., Tapley, B. D., and Ries, J. C.: Deceleration in the Earth's oblateness, J. Geophys. Res., 118, 740–747, doi:10.1002/jgrb.50058, 2013a. 9790

Cheng, M. K., Tapley, B. D., and Ries, J. C.: Geocenter variations from analysis of SLR data, in: Reference Frames for Applications in Geosciences, International Association of Geodesy Symposia, 4–8 October 2010, Marne-La-Vallee, France, vol. 138, 19–26, 2013b. 9790, 9797, 9798, 9816

GMDD
8, 9769–9816, 2015

CC BY

Crossley, D., de Linage, C., Hinderer, J., Boy, J. P., and Famiglietti, J.: A comparison of the gravity field over Central Europe from superconducting gravimeters, GRACE and global hydrological models, using EOF analysis, Geophys. J. Int., 189, 877–897, doi:10.1111/j.1365-246X.2012.05404.x, 2012. 9792

de Boer, B., Stocchi, P., and van de Wal, R. S. W.: A fully coupled 3-D ice-sheet–sea-level model: algorithm and applications, Geosci. Model Dev., 7, 2141–2156, doi:10.5194/gmd-7-2141-2014, 2014. 9771, 9780

Douglas, B. C., Cheney, R. E., Miller, L., Carter, W. E., and Robertson, D. S.: Greenland Ice Sheet: Is it growing or shrinking?, Science, 248, 288, 1990. 9795

Drygalski, E. V.: Die Geoid-Deformation der Kontinente zur Eiszeit, PhD thesis, Zeitschrift der Gesellschaft für Erdkunde zu Berlin, Berlin, Germany, 1887. 9770

Farrell, W. E. and Clark, J. A.: On postglacial sea level, Geophys. J. Roy. Astr. S., 46, 647–667, 1976. 9771, 9773, 9774, 9776, 9786, 9787, 9798

Gagliardini, O. and Zwinger, T.: The ISMIP-HOM benchmark experiments performed using the Finite-Element code Elmer, The Cryosphere, 2, 67–76, doi:10.5194/tc-2-67-2008, 2008. 9771, 9772

Gardner, A. S., Moholdt, G., Cogley, J. G., Wouters, B., Arendt, A. A., Wahr, J., Berthier, E., Hock, R., Pfeffer, W. T., Kaser, G., Ligtenberg, S. R. M., Bolch, T., Sharp, M. J., Hagen, J. O., van den Broeke, M. R., and Paul, F.: A reconciled estimate of glacier contributions to sea level rise: 2003 to 2009, Science, 340, 852–857, doi:10.1126/science.1234532, 2013. 9789, 9796

Gasperini, P. and Sabadini, R.: Finite element modeling of lateral viscosity heterogeneities and post-glacial rebound, Tectonophysics, 179, 141–149, 1990. 9779

Geuzaine, C. and Remacle, J. F.: Gmsh: a three-dimensional finite element mesh generator with built-in pre- and post-processing facilities, Int. J. Numer. Meth. Eng., 79, 1309–1331, 2009. 9780, 9810

Gomez, N., Pollard, D., and Mitrovica, J. X.: A 3-D coupled ice sheet – sea level model applied to Antarctica through the last 40 ky, Earth Planet. Sc. Lett., 384, 88–99, 2013. 9771, 9780

Gross, R. S.: The excitation of the Chandler wobble, Geophys. Res. Lett., 27, 2329–2332, 2000. 9777

Hay, C. C., Morrow, E., Kopp, R. E., and Mitrovica, J. X.: Probabilistic reanalysis of twentieth-century sea-level rise, Nature, 517, 481–484, doi:10.1038/nature14093, 2015. 9789

GMDD
8, 9769–9816, 2015

A new approach to solving the sea-level equation

S. Adhikari et al.

CC BY

Hecht, F.: BAMG: Bidimensional Anisotropic Mesh Generator, Tech. rep., FreeFem++, University Pierre et Marie Curie, France, 2006. 9780, 9810
Ivins, E. R., James, T. S., Wahr, J., O. Schrama, E. J., Landerer, F. W., and Simon, K. M.: Antarctic contribution to sea level rise observed by GRACE with improved GIA correction, J. Geophys. Res., 118, 3126–3141, doi:10.1002/jgrb.50208, 2013. 9789, 9790
James, T. S. and Ivins, E. R.: Predictions of Antarctic crustal motions driven by present-day ice sheet evolution and by isostatic memory of the Last Glacial Maximum, J. Geophys. Res., 103, 4993–5017, 1998. 9792
Jevrejeva, S., Grinsted, A., and Moore, J. C.: Upper limit for sea level projections by 2100, Environ. Res. Lett., 9, 104008, doi:10.1088/1748-9326/9/10/104008, 2014. 9789, 9795
Johnston, P.: The effect of spatially non-uniform water loads on predictions of sea level change, Geophys. J. Int., 114, 615–634, 1993. 9774
Kendall, R. A., Mitrovica, J. X., and Milne, G. A.: On post-glacial sea level – II. Numerical formulation and comparative results on spherically symmetric models, Geophys. J., 161, 679–706, doi:10.1111/j.1365-246X.2005.02553.x, 2005. 9771, 9773
King, M. A., Bingham, R. J., Moore, P., Whitehouse, P. L., Bentley, M. J., and Milne, G. A.: Lower satellite-gravimetry estimates of Antarctic sea-level contribution, Nature, 491, 586–589, doi:10.1038/nature11621, 2012. 9789
Kuhlmann, J., Dobslaw, H., and Thomas, M.: Improved modeling of sea level patterns by incorporating self-attraction and loading, J. Geophys. Res., 16, C11036, doi:10.1029/2011JC007399, 2011. 9771
Lambeck, K.: The Earth's Variable Rotation: Geophysical Causes and Consequnces, Cambridge Univ. Press, Cambridge, UK, 1980. 9776, 9777, 9778, 9779, 9793, 9795, 9807
Larour, E., Seroussi, H., Morlighem, M., and Rignot, E.: Continental scale, high order, high spatial resolution, ice sheet modeling using the Ice Sheet System Model (ISSM), J. Geophys. Res., 117, F01022, 1–20, doi:10.1029/2011JF002140, 2012. 9771, 9772, 9781
Longman, I. M.: A Green's function for determining the deformation of the Earth under surface mass loads: 1. Theory, J. Geophys. Res., 67, 845–850, doi:10.1029/JZ067i002p00845, 1962. 9775
Love, A. E. H.: Some Problems of Geodynamics, Cambridge University Press, Cambridge, 1911. 9775
Martinec, Z.: Spectral-finite element approach to three-dimensional viscoelastic relaxation in a spherical earth, Geophys. J. Int., 142, 117–141, 2000. 9779

CC BY

Milne, G. A.: Refining models of the glacial isostatic adjustment process, PhD thesis, University of Toronto, Toronto, Canada, 1998. 9774, 9777, 9779

Mitrovica, J. X. and Milne, G. A.: On post-glacial sea level: I. General theory, Geophys. J. Int., 154, 253–267, doi:10.1046/j.1365-246X.2003.01942.x, 2003. 9771, 9773, 9779

Mitrovica, J. X. and Peltier, W. R.: On post-glacial geoid subsidence over the equatorial ocean, J. Geophys. Res., 96, 20053–20071, doi:10.1029/91JB01284, 1991. 9771, 9779, 9786

Mitrovica, J. X., Wahr, J., Matsuyama, I., Paulson, A., and Tamisiea, M. E.: Reanalysis of ancient eclipse, astronomic and geodetic data: a possible route to resolving the enigma of global sea-level rise, Earth Planet. Sc. Lett., 243, 390–399, 2006. 9815

Mitrovica, J. X., Gomez, N., and Clark, P. U.: The sea-level fingerprint of West Antarctic collapse, Science, 323, 753, doi:10.1126/science.1166510, 2009. 9787

Mitrovica, J. X., Gomez, N., Morrow, E., Hay, C., Latychev, K., and Tamisiea, M. E.: On the robustness of predictions of sea level fingerprints, Geophys. J. Int., 187, 729–742, doi:10.1111/j.1365-246X.2011.05090.x, 2011. 9771, 9798

Munk, W. H. and MacDonald, G. J.: The Rotation of the Earth: A Geophysical Discussion, Cambridge Univ. Press, Cambridge, UK, 1960. 9774, 9776, 9778

Orszag, S. A.: Fourier series on spheres, Mon. Weather Rev., 102, 56–75, 1974. 9787

Peltier, W. R.: The impulse response of a Maxwell Earth, Rev. Geophys., 12, 649–669, 1974. 9777

Quinn, K. J., Ponte, R. M., and Tamisiea, M. E.: Impact of self-attraction and loading on Earth rotation, J. Geophys. Res., 120, 4510–4521, doi:10.1002/2015JB011980, 2015. 9771

Ray, R. D. and Luthcke, S. B.: Tide model errors and GRACE gravimetry: towards a more realistic assessment, Geophys. J. Int., 167, 1055–1059, 2006. 9790

Ries, J. C.: Annual geocenter motion from space geodesy and models, in: 2013 Fall Meeting, AGU, San Francisco, Calif., 9–13 December 2013, Abstract G12A-06, 2013. 9797

Riva, R., Bamber, J., Lavallée, D., and Wouters, B.: Sea-level fingerprint of continental water and ice mass change from GRACE, Geophys. Res. Lett., 37, 1–6, doi:10.1029/2010GL044770, 2010. 9771, 9798

Sabadini, R., Yuen, D. A., and Boschi, E.: Polar wander and the forced responses of a rotating, multilayered, viscoelastic planet, J. Geophys. Res., 87, 2885–2903, 1982. 9776

Shepherd, A., Ivins, E. R., A, G., Barletta, V. R., Bentley, M. J., Bettadpur, S., Briggs, K. H., Bromwich, D. H., Forsberg, R., Galin, N., Horwath, M., Jacobs, S., Joughin, I., King, M. A., Lenaerts, J. T. M., Li, J., Ligtenberg, S. R. M., Luckman, A., Luthcke, S. B., McMillan, M., Meister, R., Milne, G., Mouginot, J., Muir, A., Nicolas, J. P., Paden, J., Payne, A. J., Pritchard, H., Rignot, E., Rott, H., Sandberg Sørensen, L., Scambos, T. A., Scheuchl, B., Schrama, E. J. O., Smith, B., Sundal, A. V., van Angelen, J. H., van de Berg, W. J., van den Broeke, M. R., Vaughan, D. G., Velicogna, I., Wahr, J., Whitehouse, P. L., Wingham, D. J., Yi, D., Young, D., and Zwally, H. J.: A reconciled estimate of ice-sheet mass balance, Science, 338, 1183–1189, doi:10.1126/science.1228102, 2012. 9789, 9795

Spada, G. and Stocchi, P.: SELEN: A Fortran 90 program for solving the "sea-level equation", Comput. Geosci., 33, 538–562, 2007. 9771, 9773, 9779, 9786, 9787, 9788

Spada, G., Ricard, Y., and Sabadini, R.: Excitation of true polar wander by subduction, Nature, 360, 452–454, 1992. 9776

Swenson, S. and Wahr, J.: Methods for inferring regional surface-mass anomalies from gravity recovery and climate experiment (GRACE) measurements of time-variable gravity, J. Geophys. Res., 107, 2193, doi:10.1029/2001JB000576, 2002. 9790

Swenson, S., Wahr, J., and Milly, P. C. D.: Estimated accuracies of regional water storage variations interfered from the Gravity Recovery and Climate Experiment (GRACE), Water Resour. Res., 39, 1223, doi:10.1029/2002WR001808, 2003. 9789, 9790

Takeuchi, H., Saito, M., and Kobayashi, N.: Statical deformations and free oscillations of a model earth, J. Geophys. Res., 67, 1141–1154, 1962. 9775

Tsai, V. C. and Stevenson, D. J.: Theoretical constraints on true polar wander, J. Geophys. Res., 112, B05415, doi:10.1029/2005JB003923, 2007. 9776

Velicogna, I. and Wahr, J.: Time-variable gravity observations of ice sheet mass balance: precision and limitations of the GRACE satellite data, Geophys. Res. Lett., 40, 3055–3063, doi:10.1002/grl.50527, 2013. 9789, 9791

Wahr, J., Molenaar, M., and Bryan, F.: Time-variability of the Earth's gravity field: Hydrological and oceanic effects and their possible detection using GRACE, J. Geophys. Res., 103, 30205–30230, 1998. 9789, 9790

Wessel, P., Smith, W. H. F., Scharroo, R., Luis, J. F., and Wobbe, F.: Generic mapping tools: improved version released, EOS Trans. AGU, 94, 409–410, 2013. 9785

Woodward, R. S.: On the form and position of mean sea level, United States Geol. Survey Bull., 48, 87–170, 1888. 9771, 9775

CC BY

Wouters, B., Bonin, J. A., Chambers, D. P., Riva, R. E. M., Sasgen, I., and Wahr, J.: GRACE, time-varying gravity, Earth system dynamics and climate change, Rep. Prog. Phys., 77, 116801, doi:10.1088/0034-4885/77/11/116801, 2014. 9789
Wu, P. and Peltier, W. R.: Glacial isostatic adjustment and the free-air gravity anomaly as a constraint on deep mantle viscosity, Geophys. J. Roy. Astr. S., 74, 377–449, 1983. 9771, 9773
Wu, P. and van der Wal, W.: Postglacial sea-levels on a spherical, self-gravitating viscoelastic earth: effects of lateral viscosity variations in the upper mantle on the inference of viscosity contrasts in the lower mantle, Earth Planet. Sc. Lett., 211, 57–68, 2003. 9775, 9779
Wu, X., Heflin, M. B., Ivins, E. R., and Fukumori, I.: Seasonal and interannual global surface mass variations from multisatellite geodetic data, J. Geophys. Res., 111, B09401, doi:10.1029/2005JB004100, 2006. 9797

Table 1. Constants and parameters used in this study. Solid-earth parameters are taken from Lambeck (1980).

Constant/parameter	Symbol	Value	Unit
Mean rotational velocity of earth	Ω	7.2921×10^{-5}	s^{-1}
Average density of the earth	ρ_E	5512	$kg\,m^{-3}$
Ice density	ρ_I	910	$kg\,m^{-3}$
Ocean water density	ρ_O	1000	$kg\,m^{-3}$
Chandler wobble frequency (rigid earth)	σ_r	2.4405×10^{-7}	s^{-1}
Chandler wobble frequency (elastic earth)	σ_r^*	1.6490×10^{-7}	s^{-1}
Mean equatorial moment of inertia	$\mathcal{A}$	8.0077×10^{37}	$kg\,m^2$
Polar moment of inertia	$\mathcal{C}$	8.0345×10^{37}	$kg\,m^2$
Gravitational acceleration	g	9.81	$m\,s^{-2}$
Universal gravitational constant	G	6.6738×10^{-11}	$m^3\,kg^{-1}\,s^{-2}$
Degree 2 tidal (displacement) Love number	h_2	0.6149	–
Degree 2 tidal (potential) Love number	k_2	0.3055	–
Secular (fluid) Love number	k_s	0.942	–
Mean radius of the earth	R	6.3710×10^6	m

GMDD
8, 9769–9816, 2015

CC BY

Table 2. Comparison of pseudo-spectral and mesh-based computations of the SLE. We denote element (or pixel) size by $\mathcal{P}$, number of elements (or pixels) by $\mathcal{E}$, number of vertices by $\mathcal{V}$, and the degree at which (associated) Legendre series is truncated by $\mathcal{L}$. ($\mathcal{V}$ is not relevant for pseudo-spectral approach.)

Model	$\mathcal{E}$	$\mathcal{V}$	$\mathcal{P}$ [km]	$\mathcal{L}$	Initial time[a]	SLE time[b]	Processor[c]
Mesh-based	33 102	16 553	60–1000[d]	10 000	5 min	< 1 min	Serial
Spectral	12 288	–	204	98	< 1 min	< 1 min	Serial
	49 152	–	102	196	20 min	10 min	Serial
	196 608	–	51	392	2 h	4 h	Parallel

[a] It is the model initialization time. For pseudo-spectral models, most of this time is required to compute SHs that would be of size $\mathcal{E} \times (\mathcal{L}+1)^2$. Our model mainly utilizes this time to compute Green's functions, which are of size $\mathcal{V} \times \mathcal{E}$.
[b] It is the CPU time required to solve the SLE following instantaneous melting of a hypothetical ice sheet. Pseudo-spectral models once again deal with matrices of size $\mathcal{E} \times (\mathcal{L}+1)^2$. Our model mostly deals with vectors of size $\mathcal{V} \times 1$.
[c] Both pseudo-spectral and mesh-based models are coded in Matlab® and simulated in a MacBook Pro (OS X 10.9.5). We employ Parallel Computing Toolbox™ of Matlab® with four local *workers* in parallel runs. Serial runs use a single *worker*.
[d] Our model has variable element size. For $\mathcal{L} = 10\,000$, in principle, it can capture features of size as small as ≈ 2 km at minimal computational cost as listed above (provided that the new unstructured mesh consists of similar $\mathcal{V}$ and $\mathcal{E}$).

CC BY

Table 3. Location of selected tide gauge stations, with Global Sea Level Observing System (GLOSS) ID.

ID*	GLOSS ID	Location	Latitude	Longitude
N1	28	Male, Maldives	4.17° N	73.5° E
N2	86	Mera, Japan	34.55° N	139.49° E
N3	108	Honolulu, HI	21.30° N	157.87° W
N4	158	San Francisco, CA	37.80° N	122.47° W
N5	332	Virginia Keys, FL	25.73° N	80.16° W
N6	229	Reykjavik, Iceland	64.15° N	21.93° W
N7	241	Newlyn, UK	50.10° N	5.55° W
S1	13	Durban, South Africa	29.88° S	31.03° E
S2	129	Bluff, New Zealand	46.60° S	168.35° E
S3	195	Rio de Janeiro, Brazil	22.90° S	43.17° W
S4	95	Syowa, Antarctica	69.00° S	39.60° E
S5	278	Casey, Antarctica	66.28° S	110.53° E
S6	–	Pine Is Glacier, Antarctica	75.17° S	100.00° W
S7	188	Rothera, Antarctica	67.57° S	68.13° W

* ID has the following format: $X0$, where X = N or S (for Northern and Southern Hemispheres) and 0 = 1,...,7 (see Fig. 4a for their position on the global map).

GMDD
8, 9769–9816, 2015

A new approach to solving the sea-level equation

S. Adhikari et al.

CC BY

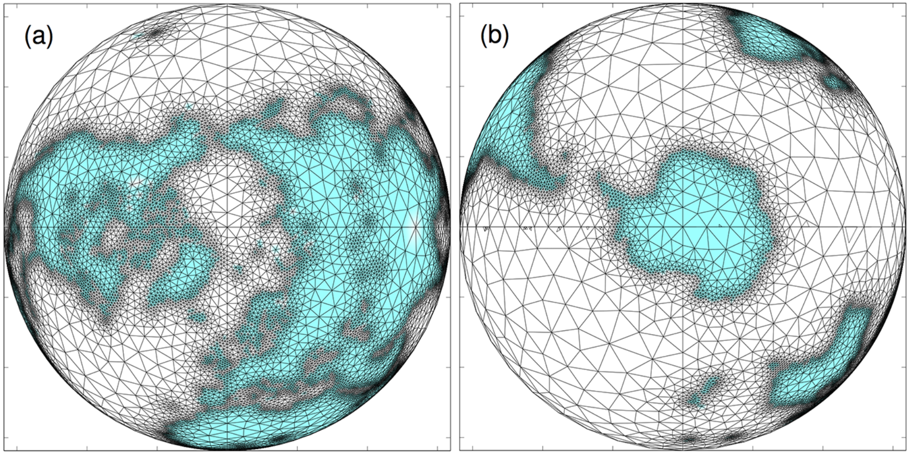

Figure 1. Example of unstructured mesh at earth surface. Both **(a)** Northern and **(b)** Southern Hemispheres are shown, with continents depicted in cyan. This mesh is generated using Gmsh (Geuzaine and Remacle, 2009), with BAMG mesh refinement algorithm (Hecht, 2006). The mesh refinement metric employed here is a function of the distance from the nearest coastline.

GMDD
8, 9769–9816, 2015

CC BY

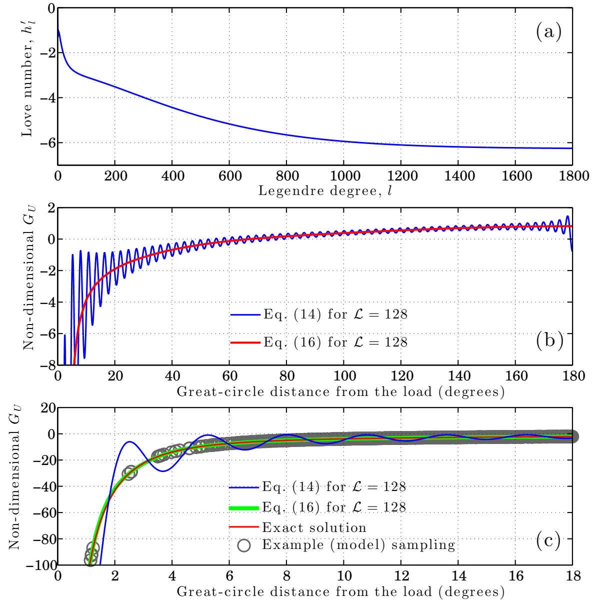

Figure 2. Parameterization of (elastic) solid earth deformation caused by surface loading. **(a)** Load Love numbers, h_l', up to 1800 Legendre degree. As $l \rightarrow \infty$, h_l' converges slowly toward a constant value. **(b)** Non-dimensional Green's function, G_U, computed by truncating the series at $\mathcal{L} = 128$. The conventional approximation (Eq. 14) produces noise, with greater amplitudes near the loading point. The problem is avoided by using the approximation given by Eq. (16). **(c)** Demonstration of model capability to accurately parameterize G_U. Solutions obtained by truncating the series (according to Eq. 16) at $\mathcal{L} = 128$ are virtually the same as exact solutions (at least beyond $\approx 1^\circ$ from the load), and these are accurately sampled by our model at an example vertex due to unit loads applied at the elemental centroids of the mesh (circles in the figure). (See Sect. 3.1 for the explanation of exact solution.) For comparison, solutions associated with Eq. (14) illustrate the ability of contemporary pseudo-spectral models to parameterize G_U.

GMDD
8, 9769–9816, 2015

A new approach to solving the sea-level equation

S. Adhikari et al.

CC BY

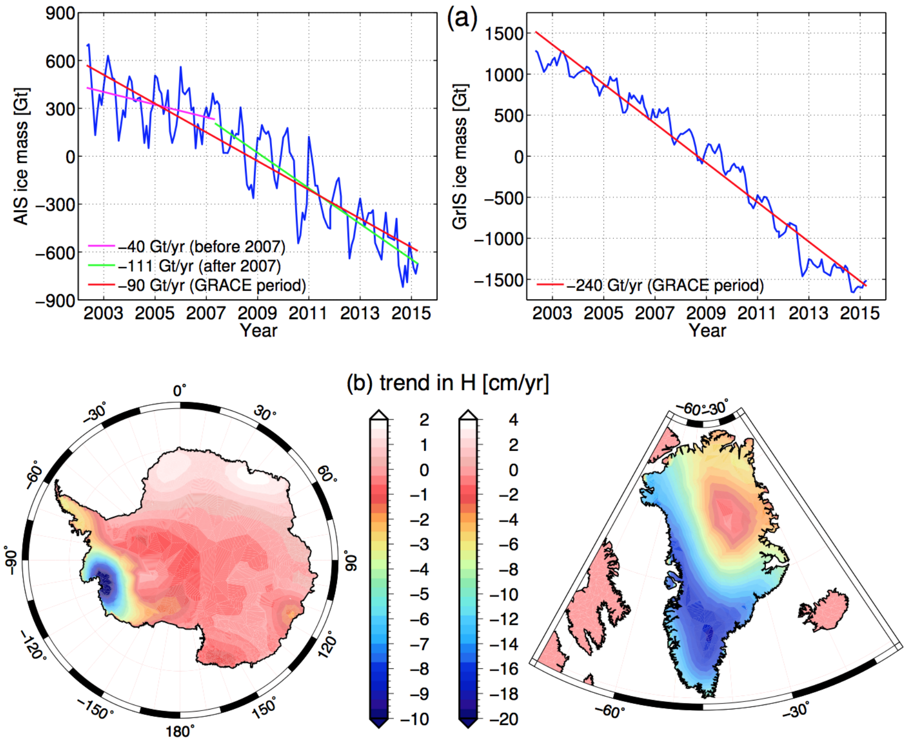

Figure 3. Summary of the GRACE data used in this study. **(a)** Ice mass change in the AIS and GrIS from April 2002 to March 2015. **(b)** Spatial distribution of rate of change in ice thickness, averaged over the GRACE period. See Sect. 4.1 for a detailed discussion of the GRACE data processing.

GMDD
8, 9769–9816, 2015

Title Page
Abstract Introduction
Conclusions References
Tables Figures
◀| |▶
◀ ▶
Back Close
Full Screen / Esc
Printer-friendly Version
Interactive Discussion

cc BY

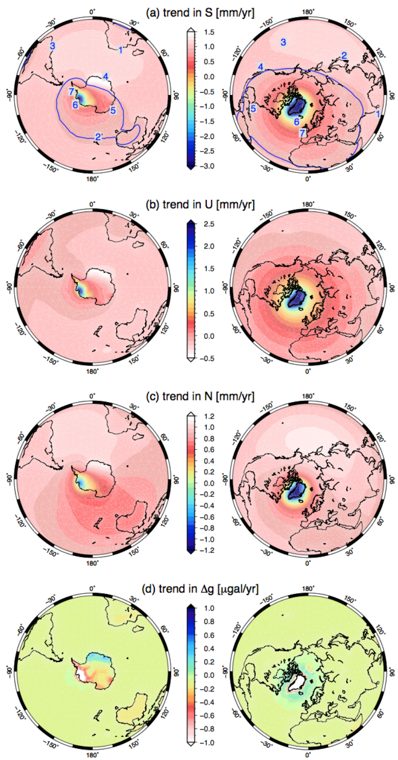

Figure 4. Some important geodetic signatures of ice sheets during the GRACE period. Rates of change in **(a)** sea level, **(b)** solid earth deformation, **(c)** geoid height, and **(d)** absolute gravity. (Notice different scale and color order in colorbars.) These results are obtained by linearly fitting the corresponding monthly solutions in a least-square sense. The blue contours in Fig. 4a represent the trend in global mean value, with magitude $\mathrm{d}S/\mathrm{d}t = 0.91\,\mathrm{mm\,yr^{-1}}$. Annotations are supplied for 14 locations in Fig. 4a (see Table 3 for their description).

GMDD

8, 9769–9816, 2015

CC BY

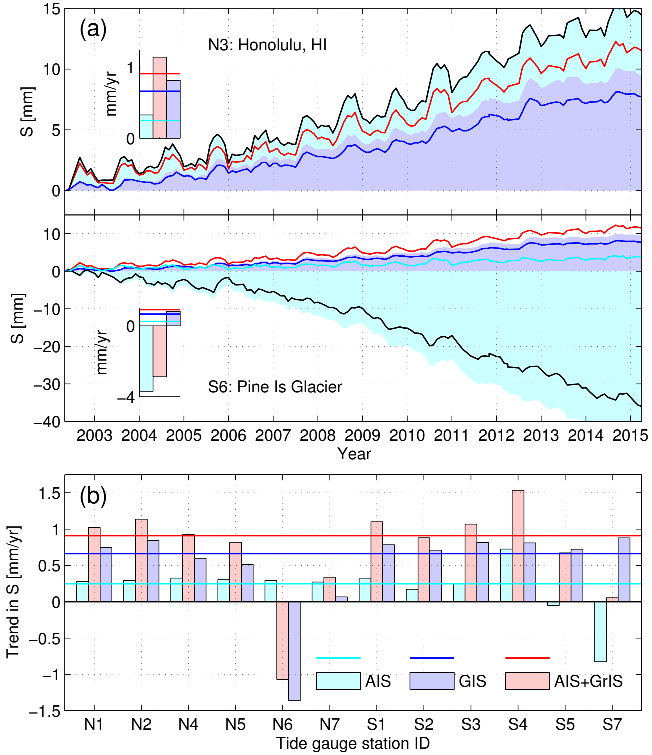

Figure 5. Magnitudes and trends of sea level change at 14 selected locations. (See Table 3 for their description and Fig. 4a for locating their position on the global map.) **(a)** Change in sea level over time at two representative sites. Average rates of sea level change are also shown in the insets. **(b)** Rate of change in sea level, averaged over the GRACE period, at 12 other locations. Cyan and blue colors (both fill and line) represent the contribution from the AIS and GrIS, respectively. The combined contributions of ice sheets are shown in red. Black lines in Fig. 5a represent the local values and all others denote the global mean values.

CC BY

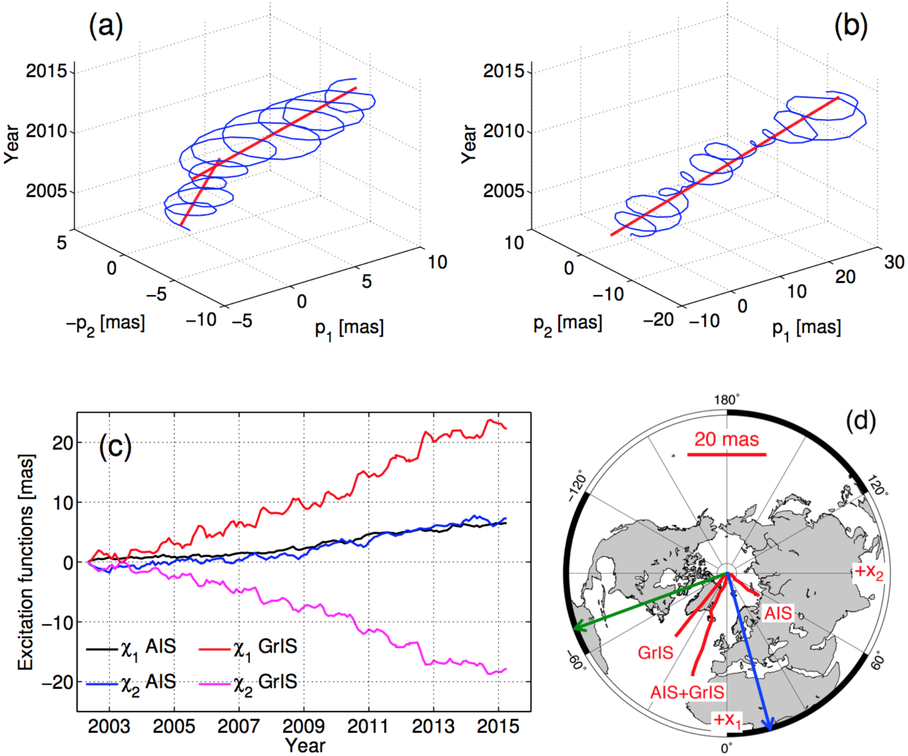

Figure 6. Polar motion during the GRACE period. Monthly pole positions (with respect to April 2002), (p_1, p_2), excited by **(a)** AIS and **(b)** GrIS mass loss in the right-handed coordinate system (x_1, x_2) (see Fig. 6d). Red lines show the average drift directions. A kink is apparent for the AIS. **(c)** Mass excitation functions, χ_1 and χ_2, associated with individual ice sheets. **(d)** Annual pole positions, after removing Chandler wobbles, with respect to the 2002 position. For comparison, the observed long-term (green arrow; Mitrovica et al., 2006) and recent (2005–2011; blue arrow; Chen et al., 2013) drift directions are also shown. Note that 1 mas ≈ 3.09 cm.

GMDD
8, 9769–9816, 2015

A new approach to solving the sea-level equation

S. Adhikari et al.

CC BY

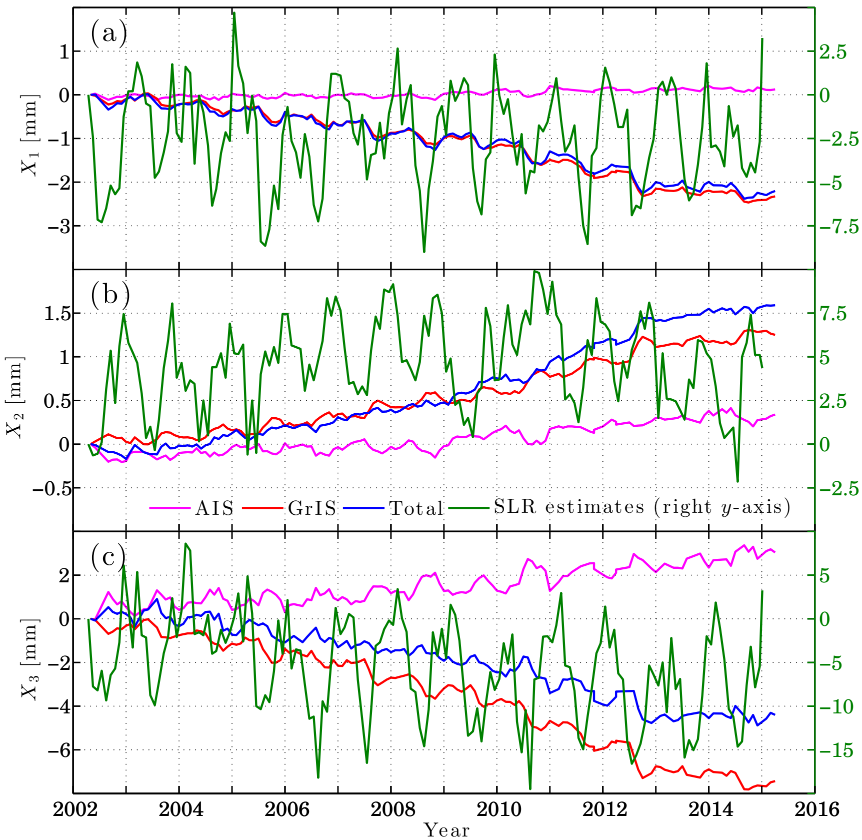

Figure 7. Geocentric motion during the GRACE period. The CM-CF shift, with respect to the April 2002 position, along the **(a)** x_1, **(b)** x_2, and **(c)** x_3 directions in a right-handed Cartesian system. (See Fig. 6d for positive sense of horizontal axes; the vertical axis, x_3, is positive out of the north pole.) Note that different scales are used (in the right y axis) for the SLR based estimates (Cheng et al., 2013b).

GMDD
8, 9769–9816, 2015